Dibris

iit
ISTITUTO ITALIANO
DI TECNOLOGIA

UNIVERSITÀ DEGLI STUDI DI GENOVA

PhD Program in Bioengineering and Robotics

Curriculum: Bionanotechnology

Cycle: XXXII

Bead Mediated Microscopy:
from high resolution microscopy to nano-Raman

Student:
Claudio Biagini

Tutors:
Dr. Francesco De Angelis
Dr. Francesco Tantussi

Contents

Introduction

Solid-state physics, material science, as well as biology, need continuously more and more information from their samples. High spatial resolution information such as optical or electrical properties, chemical species identification as well as topography are important information that optical microscopy or Scanning Probe Microscopy (SPM) can provide. Although electron microscopy (SEM and TEM) certainly assumes a position of absolute importance in the field, its cost and its need to be used by highly specialized personnel still make it an instrument of limited everyday use. On the contrary, probe microscopy has now become of very high diffusion in research labs. To develop my thesis I focused myself on three main and somehow related microscopy techniques: high resolution Raman microscopy,[1–4] Scanning Near-field Optical Microscopy (SNOM),[5] and Tip Enhanced Raman Spectroscopy (TERS).[6] All of them are state-of-the-art on surface optical analysis techniques but still present relevant limits; among others, respectively: spatial resolution, local power density, complexity and field of applicability. My approach wants to combine some aspects of these techniques to go beyond their limits.

Raman spectroscopy is a powerful optical technique,[1–4] which measures the inelastic scattering of an incoming EM radiation due to the vibrational modes of the molecules present on the surface of a sample. Thanks to its high specificity, it is very powerful in identifying the chemical components of a sample. Several organic and inorganic molecules have their typical Raman spectral peaks, hence, by the Raman spectra, it's possible to provide a qualitative and quantitative analysis of the elements of a sample. High spatial resolution Raman setups uses the combination of a confocal microscope with a spectrometer assisted by a series of long pass and band pass filters. Despite its extreme versatility, basing Raman spectroscopy on a confocal system also constrains it to acquire its limit in spatial resolution determined by the limit of diffraction[7,8].

To overcome this limit the most used techniques in SPM are Scanning Near-field Optical Microscopy (SNOM) and Tip Enhanced Raman Spectroscopy (TERS).

Both of them exploits evanescent field, which is an electric field that is created by oscillating charges and/or currents and does not propagate in the far field as a classical electromagnetic wave, but is spatially concentrated very near to its source. This confinement allows to obtain field sources definitely smaller than in confocal systems.

In SNOM technique, the excitation light is focused through an aperture smaller than the wavelength, creating an evanescent field strongly localized near the aperture itself. Scanning the sample in this near range brings the spatial resolution down to the aperture dimension.[5]

The main disadvantage of aperture SNOM is that the overall optical efficiency of probes is very low. The excitation power cannot be too high in order to prevent any damage of the probe, hence the energy that reaches the sample is usually not enough for Raman analysis.

TERS instead is more suitable for this purpose. It basically exploits Surface Enhanced Raman Spectroscopy (SERS) principles, using a laser irradiated gold sharp tip to obtain a local enhancement at its apex. Its good efficiency permits to analyze Raman effects with a spatial super-resolution, but, on the other hand, TERS probes usually lack of reproducibility and require very skilled and specialized users.[6]

My PhD project has been focused to investigate and optimize an original approach to perform high resolution optical microscopy and Raman spectroscopy, well below the diffraction limit. The concept is to exploit the optical proprieties of a dielectric micro bead lens to achieve a powerful nanoscale near field confinement of light and the Scanning Probe Microscopy (SPM) technique to scan a sample to acquire optical maps. When a dielectric micro bead is hit by an Electromagnetic (EM) wave its effect is to transmit and concentrate the incident EM radiation in a specific area called nanojet, at first glance similar to that created with a standard lens. Some optical proprieties of the nanojets have been already introduced in the literature[9–11], but their application in the world of SPM,[12,13] their employment in Raman microscopy and their combination with nanostructures to improve the spatial resolution are novel features whose investigation is promising. I gave to this technique the name of Beam Mediated Microscopy (BeMM).

The combination of super resolution bead mediated SPM with Raman spectroscopy opens interesting perspectives about powerful surface analysis for samples that need a versatile optical probe with a high spatial resolution and soft interaction with the sample, like soft matter substrates or biosamples.

To briefly sum up the work done during my PhD, here there are some key points developed during the project:

- Investigate the optical proprieties of a microscale silica bead embedded in an Atomic Force Microscopy (AFM) cantilever.
- Obtain a simultaneous AFM and high resolution Raman microscope, combining the Raman spectroscopy technique with the proprieties of the bead probes.
- Study how to create from the bead probes a Near Field (NF) optical source with nanoscale confinement, which I called SNOM-BeMM (S-BeMM).
- Obtain a near field scanning probe suitable for super resolution Raman analysis in reflection mode.
- Produce some optical maps to demonstrate BeMM and S-BeMM applicability.

State of the Art

Raman microscopy

Raman microscopy[1–4] is an optical technique which measures the inelastic scattering components of an incoming EM radiation, applicable to identify the chemical components of a specimen. Several organic and inorganic molecules have their typical Raman peaks, hence, by the Raman spectra, it's possible to provide a qualitative and quantitative analysis of the elements of a sample as well as local stress, aggregations, etc.

Raman effect

Raman scattering is an inelastic optical process, where the energy of an incoming photon changes, mainly, as a consequence of its interaction with the vibrational phonons of the sample. Raman scattering is omnidirectional and we call Stokes line when the energy of the scattered photon is lower than the exciting one and anti-Stokes when is the reverse, see Figure 1.

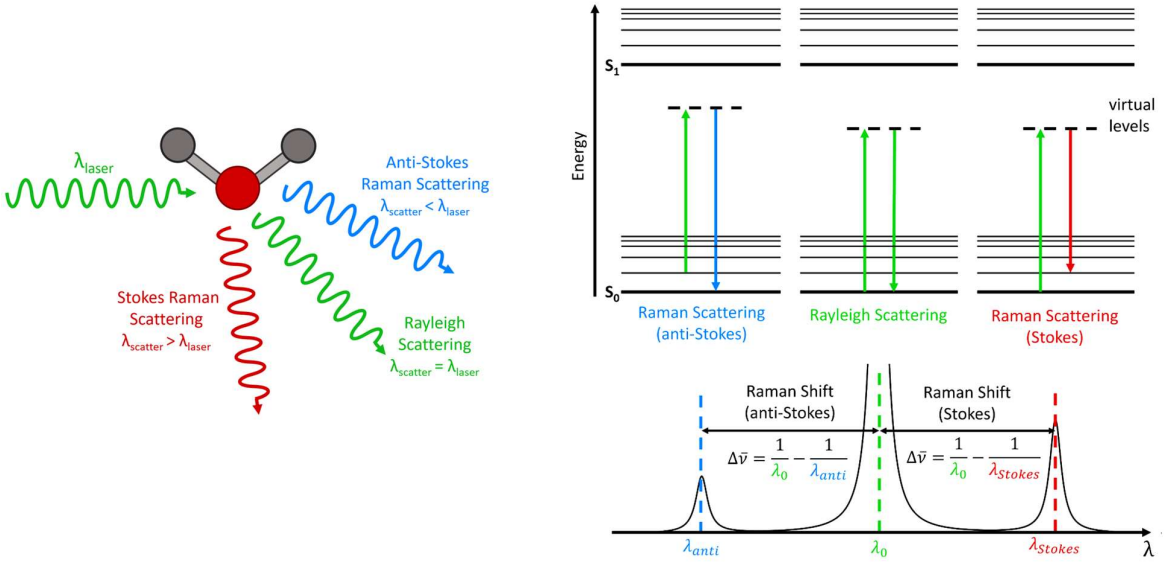

Figure 1 – Graphical representation of the Rayleigh (elastic) and Raman scattering interactions with a molecule and their energy diagram. Images taken from ref.[14]

The energy change of the scattered photon is discrete and is directly related to the vibrational properties of the specimen. The properties of the vibrational modes are basically determined by mass, bond type and symmetry of the constituting atoms in the elemental unit specimen.

The energy shift of the scattered photons can be measured by analyzing the energy spectrum of the inelastically scattered light. Peaks in a Raman spectrum correspond to certain vibration modes in the sample, and their energy measures the frequency of the corresponding atomic normal modes. Patterns of Raman peaks often form clear "spectroscopic fingerprints" of the different materials, allowing Raman spectroscopy to investigate the specimen chemical composition.[3,4]

Moreover, the presence of defects, impurities, inhomogeneities or mechanical stress affect the atom vibrational properties, and these modifications lead to slightly different Raman peak positions, noticeable in the Raman spectrum.

For all these reasons, Raman spectroscopy has proven to be a powerful technique for studying materials in a wide variety of cases, ranging from organic to inorganic materials.[1,2]

It is named after Sir Chandrashekhara Venkata Raman, who first experimentally demonstrated it and won the Nobel Prize for Physics in 1930.

Micro Raman

Raman microspectroscopy involves a high resolution optical microscope integrated with a Raman spectrometer, which is often based on a tunable monochromator combined with long pass filters and a sensitive photodetectors array (CCD or sCMOS cameras). Figure 2 shows a scheme of a typical Raman optical system.

This allows to acquire Raman spectra by microscopic areas, obtaining spectroscopic scanning maps of the investigated sample.

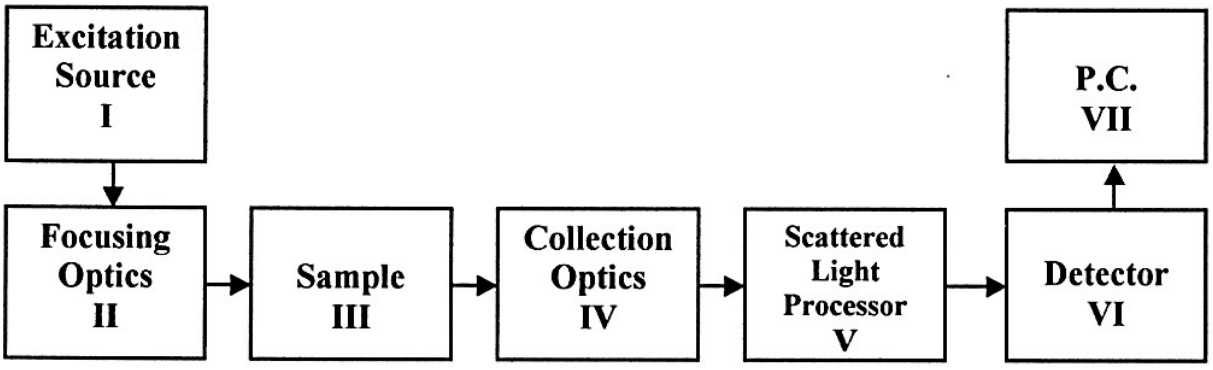

Figure 2 – Raman optical system scheme. Image taken from ref.[2]

The sample under Raman scattering investigation is irradiated through an objective with an intense light beam, usually a continuous-wave laser beam. Scattered light is generated mainly by Rayleigh scattering, but a smaller part (five-six order of magnitude less) also by Raman scattering. While Rayleigh scattering leads to light with unchanged optical frequency, Raman scattering produces scattered components with substantially modified optical frequencies. Those frequency-shifted components must be analyzed with a selective and sensible optical system.

The obtained Raman spectra are usually not shown with absolute optical frequencies on the horizontal axis, but rather with differences of wavenumber (understood as inverse wavelength) in units of cm^{-1}. Those differences are proportional to the difference in optical frequency or photon energy.

Vibration modes of molecules are often dominantly associated with vibrations of certain chemical bonds, and then have vibration frequencies which are characteristic for those bonds. For example, C-H bonds typically correspond to wave numbers around 2800 to 3200 cm^{-1}, while C-O double bonds are at roughly 1700 cm^{-1}.[15]

Raman scattering is a relatively weak process: the Raman peaks intensities typically are high at most 10^{-5} respect to the light scattered via Rayleigh scattering. Therefore, a critical point is to suppress the disturbing effect of the far stronger Rayleigh-scattered light, in order to perform a measurement with a reasonable signal-to-noise ratio.[16] Usually one or more optical filters (e.g. long pass, band pass and notch filters) are used for strongly attenuating Rayleigh-scattered light before entering the spectrometer.

Microbeads

Microbeads, or microspheres, are small spherical solid particles with dimensions from 1 µm to 1 mm. They can be made of various natural or synthetic materials, like glass, polymer, metal, and ceramic materials, hence they vary widely in density, surface properties and optical properties. Microbeads can have different quality, sphericity, uniformity, particle size and particle size distribution. Thus, their applications depend on all these properties.

For example, polystyrene microbeads are mainly used in biomedical applications. Polyethylene ones are used as filler and, thanks to the possibility to be colored and/or fluorescent, they are used in fluid flow analysis and microscopy techniques. Glass microspheres are employed as filler and volumizer for weight reduction, retro-reflector, additive for cosmetics and adhesives. Ceramic microspheres are used primarily as grinding media.

If the size of a dielectric sphere is larger than the illuminating source wavelength, the analysis of its focusing properties can be done with a geometrical optics approach, considering it, in the first approximation, as a thick lens.[17,18]

In spherical geometry the only variables of the lens determining the effective focal length, f, of the system, are the refractive index contrast between the lens and the surrounding medium, n', and the diameter, D. The effective focal length can be calculated with this equation: $f = n' D/4\,(n' - 1)$.

It follows that when $n' > 2$, $f < D/2$, that means that the light will be focused inside the lens; when $n' = 2$, $f = D/2$, hence the light is focused at the back surface of the sphere; and when $n' < 2$ the $f > D/2$, so the light will be focused outside the lens.

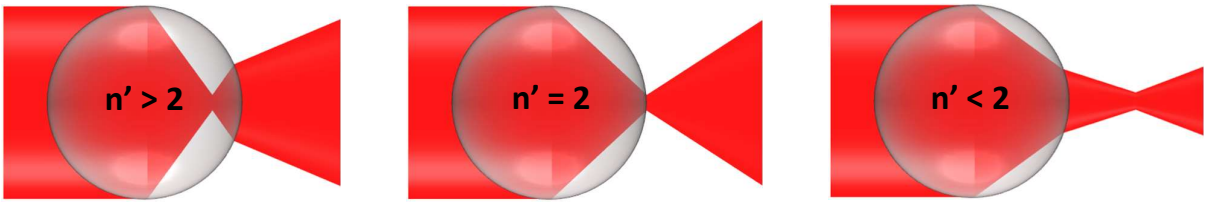

Figure 3 – Sketch of the focus positions dependence from the refractive index contrast between the bead and the surrounding medium n'.

Numerical Aperture (NA) of lenses is defined by the following formula: $NA = n\,sin\theta = n\sin[\arctan(D/2f)] \approx n\,D/2f$, where n is the lens refractive index, D in our case is the bead diameter and Θ is the maximal half-angle of the cone of light that can enter or exit the bead.[19] Accordingly with these formulas, the higher the bead refractive index, the higher NA is possible to reach.

These systems have been studied by various groups, as illustrated in next chapter. In particular several theoretical and simulation studies have been done about their particularly interesting focusing effect, called photonic nanojet.

In our case we make the light of a HeNe laser (λ = 632.8 nm) interact with 4.9 microns silica beads. Silica refractive index is ≈ 1.55, so it's not exceptionally high. However, it's a very common and cheap material, features that are relevant for mass production. Applying the previous formulas we obtain a theoretical NA of ~1.1 for this particular spherical lens, in good agreement with the experimental characterization results.[12]

Photonic Nanojets

The first studies that predicted photonics nanojets considered microcylinders[20], and only later they studied microspheres. First of all, it was calculated that illuminating by a plane wave a wavelength-scale dielectric cylinder, a localized nanoscale photonic jets is generated at its shadow-side surfaces. They evolve for different refractive indexes of cylinders, making them emerging out to the back surface of the cylinder. Their waists are less than λ/2 and they propagate over several optical wavelengths without significant diffraction.[11,20] These optical effects were studied by 2D Finite-Difference Time-Domain (FDTD) computational solutions to Maxwell's equations (Mie theory). Some results can be seen in Figure 4.

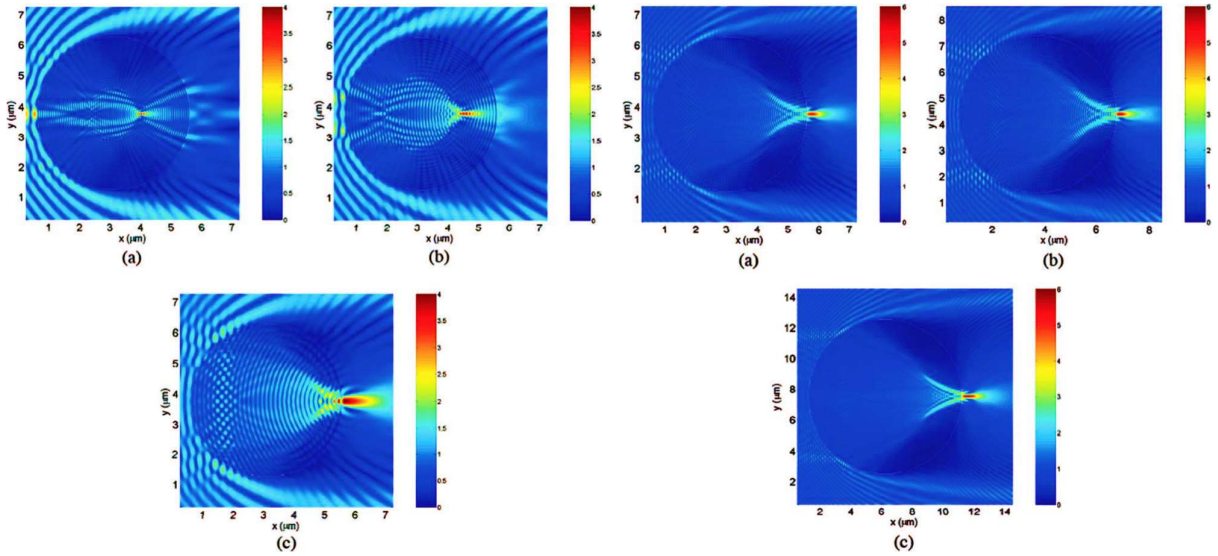

Figure 4 – Left - Visualizations of the evolution of a photonic nanojet as the refractive index of a plane-wave-illuminated circular dielectric cylinder decreases. The FDTD-computed envelope of the sinusoidal steady-state electric field is visualized for a d = 5 μm diameter cylinder of uniform refractive index n_1 embedded within an infinite vacuum medium of refractive index n_2 = 1. Light of wavelength λ_2 = 500 nm propagates from left to right in medium 2. (a) n_1 = 3.5; (b) n_1 = 2.5; (c) n_1 = 1.7. Right - Visualizations of the generation of photonic nanojets for three different combinations of d, n_1, n_2, and λ_2. (a) d = 5 μm, n_1 = 3.5, n_2 = 2.0, λ_2 = 250 nm; (b) d = 6 μm, n_1 = 2.3275, n_2 = 1.33, λ_2 = 300 nm; (c) d = 10 μm, n_1 = 2.3275, n_2 = 1.33, λ_2 = 300 nm. Images taken from refs. [11,20]

Later, the investigation has moved from 2D microcylinders to 3D. With the proper refractive indexes, the nanojet's minimum beamwidth can be even smaller, ~λ/3 for microspheres, and with a greater intensity that can increase by two order of magnitude respect the incident wave (see Figure 5).

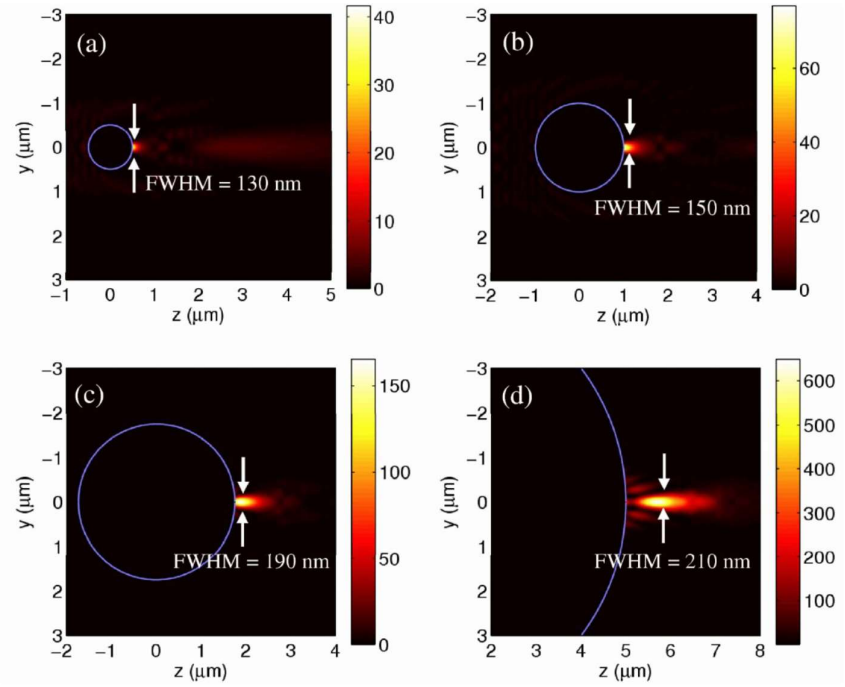

Figure 5 - Visualizations of the photonic nanojets generated by illuminating dielectric microspheres of refractive index n_μ = 1.59 in vacuum with a λ = 400 nm, x-polarized, z-propagating plane waves of unit intensity. The near fields are computed using the Mie series. (a) d_μ = 1 μm microsphere diameter; (b) d_μ = 2 μm; (c) d_μ = 3.5 μm; (d) d_μ = 8 μm. Images taken from refs. [11,21]

After the theoretical studies mentioned before, Ferrand et al. conducted experiments to directly observe such photonic nanojets.[22] They were able to reconstruct the image of a photonic nanojet through the analysis of the intensity mapped at different image planes below the bead.

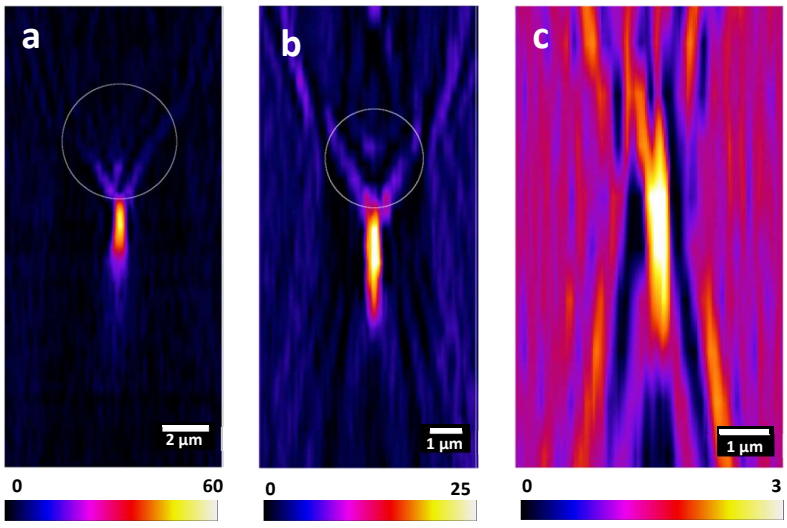

Figure 6 - Direct observation of photonic jets produced by latex microspheres illuminated by plane waves of λ=520 nm. (a) Sphere diameter, D=5 μm. (b) D=3 μm. (c) D=1 μm. Scale bars are different. Images taken from ref.[22]

In Figure 6 the intensity maps of dielectric microspheres illuminated by visible light are shown. Sub-wavelength nanojets with enhancement factors up to 60x are produced, in good agreement with numerical simulations they made for these beads.[22]

Summing up, a photonic nanojet is a narrow, high-intensity, non-evanescent propagating light beam emerging from the shadow-side of an illuminated lossless dielectric microsphere (or microcylinder) of diameter larger than λ. Simulations and experiments support that the minimum beamwidth of microsphere nanojet can be particularly small, $\sim\lambda/3$,[11,20,21] with an intensity that can reach values more than two orders of magnitude more than the illuminating wave. Field intensity and distribution are dependent on microbead size and on refractive index contrast with the surrounding medium. Higher index contrast increases the focalization and squeeze photonic jet.[23–25]

For a more detailed numerical analysis, has been used an eigenfunction solution of the Helmholtz equation which has been recast into a Debye series.[9] Propagating wave contributions are predominantly to the nanojet, but the evanescent field contributions, created by the illuminated microsphere, enhance and sharpen the nanojet's field distribution. Overall, nanojet characteristics were concluded to arise from a "unique combination of features" in the angular spectrum involving the phase distribution and the finite content of propagating and evanescent spatial frequencies. Regarding the spatial and spectral properties of the three-dimensional photonic nanojet, the contributions from all spatial frequency components, both propagating and evanescent, was quantitatively evaluated in a framework employing rigorous Lorentz-Mie theory.[10]

The high intensity of nanojet helps to identify nanoparticles and nanometric structures, increasing a lot the optical signal. Inserting a nanoparticle with diameter d within a nanojet, the far-field backscattered power of the illuminated microsphere is perturbed by an amount that varies as d^3. This perturbation is much slower than the d^6 dependence of Rayleigh scattering for the same isolated nanoparticle. For example, the measured far-field backscattered power of a 3 μm diameter microsphere could double if a 30 nm particle is inserted into the nanojet, despite the nanoparticle is 10^4 times smaller than the microsphere cross-section area.[11] The nanojet projects the presence of the nanoparticle to the far field.

These properties combine to afford potentially important applications of photonic nanojets for detecting and manipulating nanoscale objects, subdiffraction-resolution nanopatterning and nanolithography, low-loss waveguiding and ultrahigh-density optical storage, as recapped in ref.[11]

An important field that is still little considered for the employment of nanojets is Raman microscopy. As I already said in previous chapters, performing Raman analysis below the diffraction limit is difficult, complicated and expensive. This type of measurement needs an

intense and very confined excitement light, making microbeads and nanojets promising tools for reaching good performances.

It's important to highlight that most of the theoretical and proof-of-concept results have been reached considering planar waves as reference. Instead, a more challenging competitor should be the laser beam of an optical objective, which is more realistic if we consider common characterization techniques.

Beads for wide range of applications

The formation of a high enhanced sub-diffraction limited volume in an easy way with a low cost setup leads to a wide range of potential applications. I would like to list just few of them here more for the purpose of turning on the reader's attention than to be exhaustive in their analysis.

Several polystyrene touching microspheres have been used as low-loss optical waveguiding, thanks to the propagation of nanojet-induced modes.[26] In a molecular dye solution with a suspension of silica microspheres has been experimentally observed a non-linear enhancement of two-photon excited fluorescence, due to the nanojets.[27] The localized optical electric field within photonic nanojets of self-assembled silica microspheres enhances Raman scattering.[28] A monolayer of self-assembled silica of polystyrene microspheres can direct-write periodic nanopatterns with a fast and cheap approach.[29]

My experience with beads began with an approach similar to the previous one on high-resolution optical lithography. I studied how a microbead mounted on top of an AFM cantilever can be exploited to write a desired pattern on the optical resist with very high resolution.[13] Similarly, bead-on-cantilever system has been used for enhancing the spatial resolution of traditional optical systems, for imaging different sub-wavelength structures.[12]

Near Field theory from a sub wavelength aperture to SNOM and TERS

During the thesis work of my PhD the concepts of Near Field optics, evanescent wave and Scanning Near-field Optical Microscopy (SNOM) have taken a position of relevance. In this part I will give a brief overview of these concepts.

First of all, we have to make some considerations about the transmission of an electric field behind a small aperture (below diffraction limit), later we'll discuss more on its application in SNOM.

Theory of transmission from a "small" aperture

The transmission coefficient of a subwavelength hole in an infinitely thin perfectly conducting screen was first calculated rigorously by Bethe.[30] Errors in his expression for the near field were corrected in a paper by Bouwkamp.[31] The so-called Bethe/Bouwkamp model of a subwavelength aperture is important because it provides closed analytic expressions for the resulting electric and magnetic field. Although the model fails to accurately describe reality, the expressions still include the most characteristic features of the near- and far-field distribution of a realistic subwavelength aperture.

Within the Bethe/Bouwkamp model, it is expected that the transmission coefficient of a subwavelength hole should scale as a^4, where "a" denotes the aperture diameter.[30–32] An increase of the aperture diameter from 20 to 100 nm hence results in a transmission coefficient increased by a factor of 625.

For an incident plane wave, it's possible to calculate analytically the power transmission functions of the propagating field and of the evanescent wave. The calculated dependences of the power transmission functions for evanescent and propagating waves, respectively: T_x^{ev} (z) and T_x^{pr} (z) along z-axis for different values of aperture radius *R*, are shown in Figure 7;[33] for simplicity, wave amplitude is set 1.

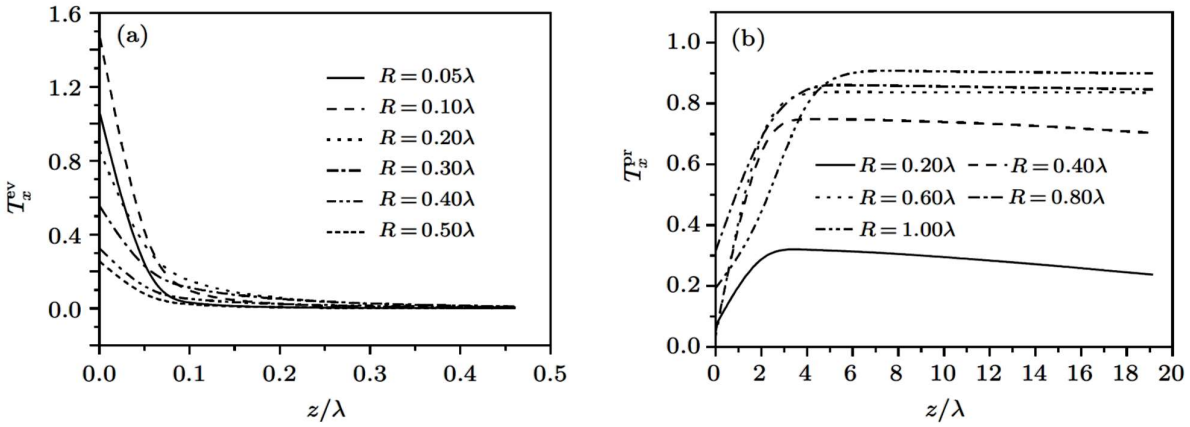

Figure 7 – Analytically calculated dependences of power transmission functions of the evanescent wave components T_x^{ev} (z) (a) and transmission function of the propagating component T_x^{pr} (z) (b) on z for different values of aperture radius R. Images taken from ref.[33]

As is well illustrated in Figure 7, the trends of T_x^{ev} (z) and T_x^{pr} (z) are correlated and show an important behavior on a scale in the order of lambda or tenths of it. The power transmission function T_x^{pr}(z) first increases to a maximal value and then nearly keeps this value or slightly decreases with the increase of z [Figure 7(b)].

Conversely, the power transmission function T_x^{ev}(z) [Figure 7(a)] decreases rapidly with the increase of z and the attenuation distance is very small (smaller than 0.3 λ).

T_x^{ev}(z) decreases around 0 as $R \geq 0.35\,\lambda$ for any z, displaying that the on-axis evanescent field exists only under the condition of the very small aperture radius. Vice versa, when $R << \lambda$, T_x^{ev}(z) reaches values also higher than 1, showing an abnormal transmission due to a very small aperture.[33]

However, working with really small apertures (< 40-50 nm) is often impossible since the overall transmission coefficient decreases dramatically with decreasing aperture size. This cannot be overcome by an increased input power due to the generally low damage threshold of the metal coating. The relevant near field signal becomes so small that the signal to noise ratio is no longer sufficient to provide reliable results. This is the reason why most near field studies today are carried out with apertures around 80-100 nm.

Let's now consider a very simple geometry: a slit in a thin, good-conducting metallic screen, illuminated at normal incidence by a plane wave with wave number $k_0 = 2\pi/\lambda$ [Figure 8(a)].[34]

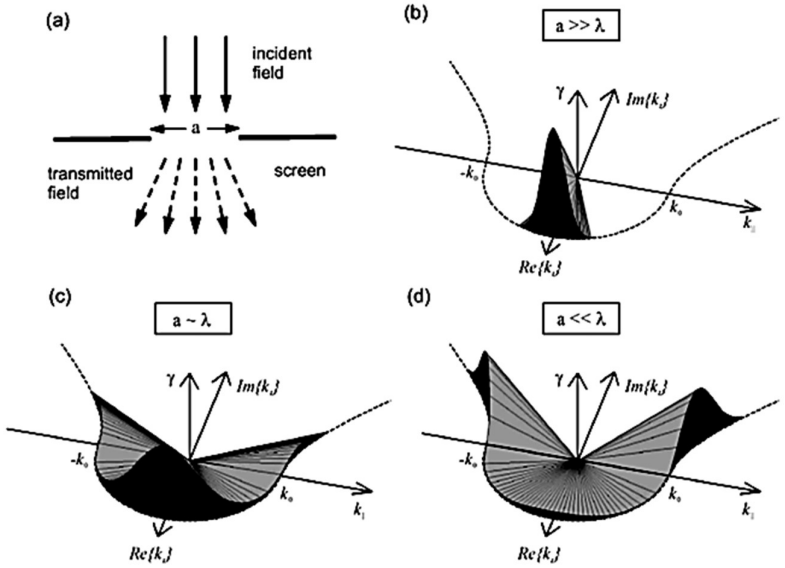

Figure 8 - Character of the electric fields behind an aperture: (a) A small aperture of size a in an infinitely thin and perfectly conducting screen is illuminated at normal incidence with a plane wave propagating in the z direction with a vector $k_z = k_0 = 2\pi / \lambda$. (b, c, d) The spectrum of the transmitted field is given for three different aperture sizes. In each case the vertical axis represents the field amplitude γ of the k vector with components (k_{II}, k_z), where the transverse component k_{II} is real and the longitudinal component k_z can be either real or imaginary. The latter corresponds to an evanescent field strongly localized at the vicinity of the aperture. The ratio of propagating and evanescent fields strongly depends on the aperture size a relative to the wavelength λ. Images taken from ref.[34]

Right behind this aperture, the transmitted field will be more or less confined to its width.[35] The character of this field is best understood by considering its angular (Fourier) spectrum.[36] The electric field distribution behind the aperture can be obtained by convoluting the angular spectrum of the incident field with the Fourier transform of the

aperture.[36] The Fourier transformation must be performed in the plane of the screen and provides an angular spectrum of plane and evanescent waves with field amplitudes γ (k_{II} , k_z). k_{II} and k_z are respectively the transverse and longitudinal components of the k vector. It's assumed that the transverse component k_{II} is real. On the other hand, the longitudinal component k_z can be either real or imaginary. It is related to k_{II} via

$$k_0^2 = k_{II}^2 + k_Z^2 \qquad (1)$$

Together, k_{II} and k_z describe the radiation properties of the plane and evanescent waves that constitute the field behind the aperture. The angular spectra for different aperture sizes are depicted in Figure 8(b-d). Field amplitudes $\gamma(k_{II}, k_z)$ concentrated at small k_{II} correspond to large apertures, whereas a distribution of $\gamma(k_{II}, kz)$ over a broad range of k_{II} values corresponds to small apertures. From Eq. (1) we see that, depending on the magnitude of k_{II}, two different types of solutions are obtained for k_z

$$k_Z = \begin{cases} \sqrt{k_0^2 - k_{II}^2} & k_{II} \le k_0 \\ i\sqrt{k_{II}^2 - k_0^2} & k_{II} > k_0 \end{cases} \qquad (2)$$

Let's consider an aperture of width a. The angular spectrum of this aperture will contain field amplitudes $\gamma(k_{II}, k_z)$ at $k_{II} = 2\pi/a$. For this value of k_{II}, the expression for the longitudinal wave vector component becomes

$$k_Z = \sqrt{\left(\frac{2\pi}{\lambda}\right)^2 - \left(\frac{2\pi}{a}\right)^2} \qquad (3)$$

Hence for $a < \lambda$, k_z becomes imaginary. The two sets of solutions described by Eq. (2) are depicted as a dashed line in Figure 8(b-d): for $|k_{II}| \le k_0$ the extremity of the k vector describes a circle in the (k_{II} , k_z) plane, with a real k_z component.

Instead, for $|k_{II}| > k_0$ the solutions follow a square-root curve, with an imaginary k_z component. A field component with an imaginary wave vector in the propagation direction corresponds to an evanescent field. It remains strongly bound to the aperture and does not propagate into the far field. The strong localization is the reason for the high resolution that can be reached in SNOM technique.[37]

For a given wavelength, the ratio of propagating and evanescent field (respectively k_z real and k_z imaginary) amplitudes in the angular spectrum strongly depends on the size a of the aperture as compared to λ [Figure 8(b-d)].

When $a >> \lambda$, the angular spectrum of the transmitted field is very similar to that of the incident field, i.e., most of the transmitted field propagates in the forward direction with a propagation vector $k_z \approx k_0$, $k_{II} \approx 0$ [Figure 8(b)]. Few field components with a small k_{II} can appear, causing a slight divergence of the beam transmitted through the aperture.

When the aperture size becomes comparable to the wavelength, the lateral confinement increases and the spectrum broadens. As a result the transmitted field diverges strongly [Figure 8(c)]. The angular spectrum of the transmitted field now also includes a small range of finite amplitudes with $|k_{II}| > k_0$.

Finally, when the aperture is much smaller than the wavelength, the spectrum of the transmitted field in the z direction becomes dominated by the evanescent components; i.e., for the vast majority of the transverse components, $k_{//}$ is larger than k_0 [Figure 8(d)]. This means that the transmitted field is strongly localized at the vicinity of the aperture and decreases rapidly away from the aperture. As a result, the far-field power emitted by the aperture decreases, while strongly confined and enhanced fields appear at the vicinity of the aperture. In Figure 9 we can see the percentages of evanescent and propagating field intensity as a function of a/λ.

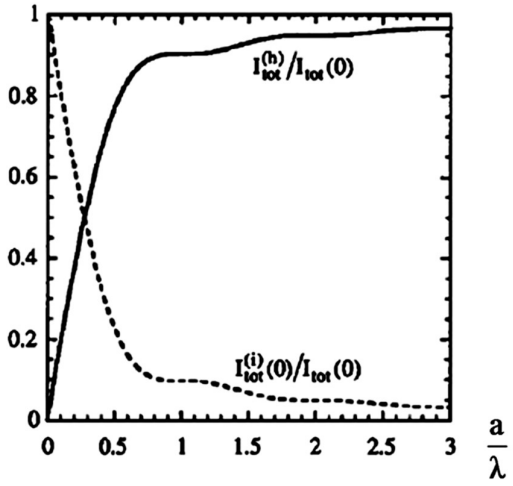

Figure 9 - Plot of the fraction of total evanescent intensity at the nanohole surface $I^{(i)}_{tot}(0)/I_{tot}(0)$ and total propagating intensity $I^{(h)}_{tot}(0)/I_{tot}(0)$ as a function of normalized slit width, a/λ. Image taken from ref.[38]

Experimental evidence for the existence of non-radiative fields close to an aperture are the ''forbidden light'' emission,[39,40] surface plasmon excitation,[41] as well as an increased fluorescence from single molecules close to an aperture.[42]

Transform the evanescent, confined, exciting field of a nanoscale aperture into a propagating EM field that carry high spatial resolution information about the sample is the mechanism on which Scanning Near-field Optical Microscopy (SNOM) technique is based.

Scanning Near-field Optical Microscopy (SNOM)

Scanning Near-field Optical Microscopy exploits a nanometric aperture or tip to convert propagating light into evanescent waves and vice versa, allowing to construct scanning optical images with nanometric resolution.

Various SNOM configurations have been classically used up to now, depending on the probe, the sample and the illumination and detection methods.[43] The probe can be defined by either an aperture or a sharp solid tip probe (in this case it's called apertureless SNOM). The probe can be used as a nano-source of light (illumination mode) that is then collected in the far field, a nano-collector of light (collection mode) that is illuminated by a far field source, or also as both near-field illuminator and collector.

SNOM measurement can be done in transmission, if the sample is transparent, or in reflection.

Figure 10 shows the most typical SNOM configurations, introduced above.

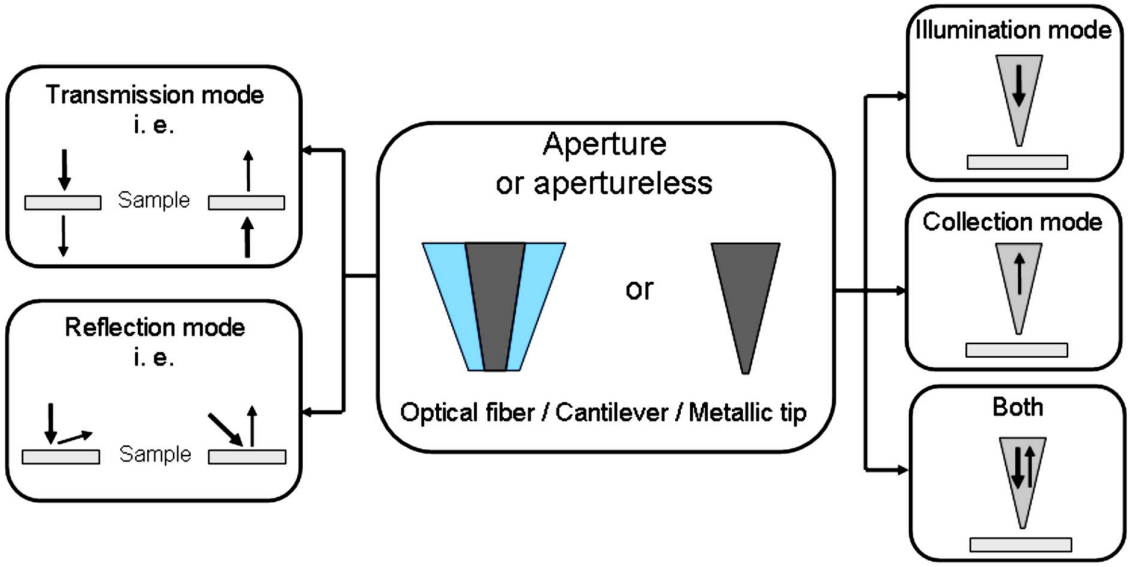

Figure 10 – Various SNOM configurations depending on the sample, the probe and the illumination/detection system. Image taken from ref.[43]

High Numerical Aperture (NA) objective lens or special optics are preferred to collect the scattered light.[40,44]

Considering the spatial and confinement characteristics of near field, it is important to combine the nano-opening with an aperture-sample gap control system. This control, common in all SPM microscopes, is based on a feedback loop. This feedback loop can exploit various parameters, the most common of which are: the amplitude or phase of a tuning fork[45–47], the current in Scanning Tunnel Microscopy (STM)[5,48–50] or the deflection of an optical cantilever. The latter, typical of AFM microscopy[51–54], is the system I adopt since the probe is a modification of an AFM cantilever. More details on AFM technique and its operating mode that I used can be found in chapter "AFM setup".

SNOM probe fabrications techniques

Several techniques have been applied to the fabrication of SNOM probes,[55,56] and few of these designs are used for commercially available tips.

As probe tips for aperture-SNOM, aluminum-coated tapered glass fibers,[57,58] and AFM cantilevers[59] with aperture hole are typically employed. The former are relatively simple to fabricate, cheaper, and definitely easier to couple to a laser source.

Fiber-based optical probes are fabricated creating a transparent taper with a sharp apex and then coating the cone walls with an opaque Cr-Al film, in order to obtain an aperture at the apex. The two main methods to prepare tapered optical fibers are: ''heating and pulling'' and chemical etching.

The first method provides smoother tips, but with low power transmission efficiency, due to a low taper angle. The second provides large taper angles, but high surface roughness and poor reproducibility. A comparison between the two typical taper angles can be seen in Figure 11(a, c), while Figure 11 (b, d) show Scanning Electron Microscopy (SEM) images of the apex regions.

As we can see in Figure 11(e), evaporating at a proper angle permits to obtain a self-aligned formation of the aperture at the fiber apex, thanks to a geometrical shadowing effect.

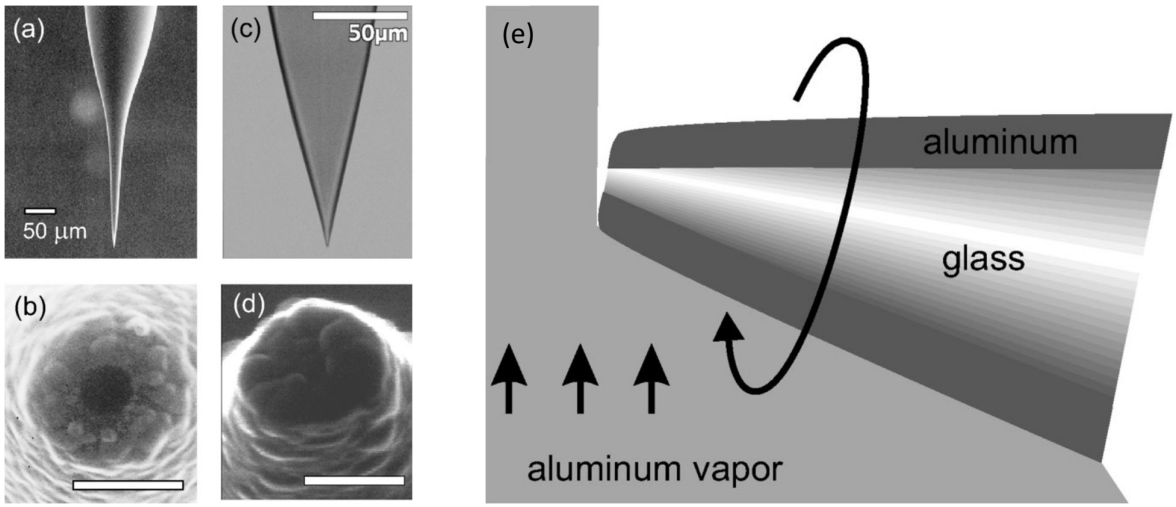

Figure 11 – Aluminum-coated aperture probes prepared by heating and pulling (a),(b) and tube etching (c),(d): (a),(c) macroscopic shape, SEM and optical image. (b),(d) SEM close-up of the aperture region, scale bar corresponds to 300 nm. e) Evaporation geometry of the aluminum coating process: evaporation takes place under an angle slightly from behind while the tip is rotating. The deposition rate of metal at the apex is much smaller than on the side walls. Images taken from refs.[34,60]

The optical signal in standard aperture-tip-based systems is quite weak due to the prevalent high power losses in the fiber tip. Besides fiber tips, other kinds of aperture probes

have been developed in order to limit the losses, which exhibit good power transmission and resolutions down to few tens of nanometers. Here are some of the most significant examples.

Micromachined cantilever-type SNOM probes [Figure 12(a)] have a more efficient light throughput than optical fiber-type probes. Their tip apex curvature can be adjusted through controlling Si oxidation process.[61]

Another kind of cantilever-type probe is a hollow metal-coated pyramid probe [Figure 12(b)].[62] The tip is made of a SiO_2 pyramid on a Si cantilever and can be directly used in a commercial AFM instrument. With a large apex angle, this type of tip exhibits a high power transmission with a spatial resolution around 100 nm.

A third example are aperture-tetrahedral tips [Figure 12(c)],[63,64] which demonstrated high spatial resolution (30 nm) with a good power transmission.

Fluorescent material located on the probe was also utilized to obtain a SNOM image. The collected signal from fluorophore-sample system is easily distinguishable from background electromagnetic wave, and as a result signal-to-noise ratio is greatly enhanced.[65,66] Other studied techniques have been for example nonlinear optics based on two-photon excited fluorescence,[67,68] and second-harmonic generation.[69,70]

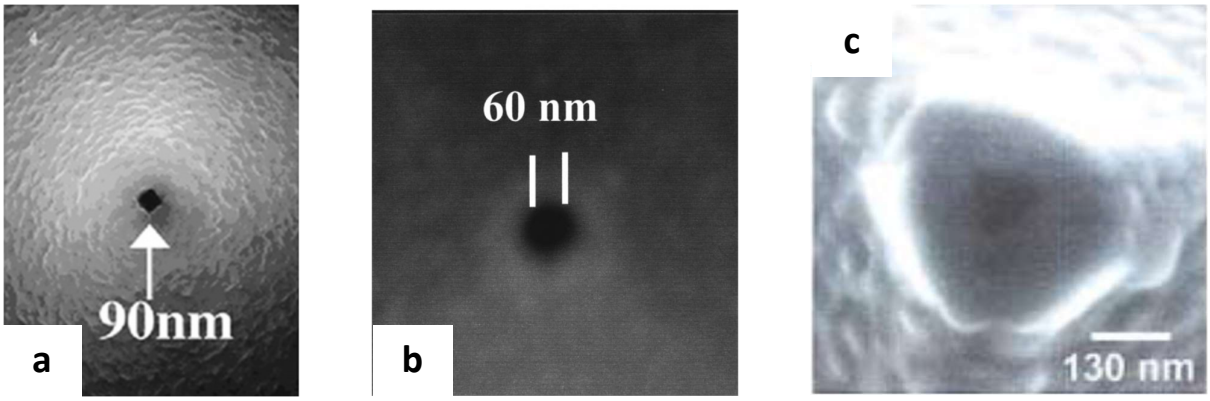

Figure 12 – (a) SEM image of tip apex made by Si micromachining. (b) Hollow silver coated pyramid structure. (c) Al-coated tetrahedral probe with a 30 nm aperture. Images taken from refs.[61–63]

The high difficult fabrication processes of these kinds of tips make them very expensive probes.

Considering the area near the aperture at the apex of a SNOM tip, the transmission coefficient depends by the part that guides light towards the subwavelength aperture. In fiber probes, the guiding part is a metal-coated tapered dielectric waveguide (Figure 13).

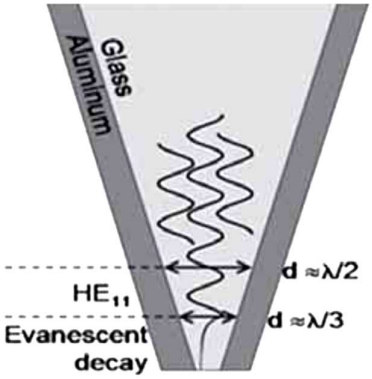

Figure 13 – Mode propagation in a tapered aluminum-coated optical fiber, with cutoff diameters. Image taken from ref.[71]

The guiding efficiency depends on the propagating modes distribution along the tapered waveguide. When the mode "feels" the proximity of the metal coating, the waveguide changes its behavior from a dielectric to a metallic hollow one filled with a dielectric.

The mode structure in the metallic waveguide leads to a reorganization of propagating modes, and causes a strong attenuation due to the back-reflection of light. These modes are functions of the dielectric core diameter.[72] When the core diameter decreases progressively the modes gradually run into cutoff, and the last that still propagates is the fundamental HE_{11} mode. The wave vector of the cutoff modes becomes imaginary and the mode field decays exponentially.

The power excluded from the propagating modes is either reflected back into the waveguide or absorbed in the metal coating, leading to a considerable heating of the metal.[73–76]

At this point, the transmission coefficient is mainly determined by the ratio between the power fraction of the cutoff modes and the HE_{11} mode still propagating power. The energy that reaches the aperture is linked to the distance between the HE_{11} cutoff diameter and the aperture, which depends on the taper angle. The larger the angle, the higher the overall transmission coefficient.[71,77]

Considering the aperture, light transmission coefficient through a small hole on a conducting sheet is proportional to $(D/\lambda)^4$, where D is the aperture diameter[30,31,78]. Hence, reducing the diameter for example from 100 to 10 nm to improve spatial resolution, the signal intensity lowers by a factor of 10^4. This low throughput problem has created a lot of difficulties in the path towards SNOM at the nano-resolution.

The easiest approach is to increase the input power. However, a too high power causes tip heating up to hundreds of degrees, which can bring to tip melting and/or sample heating.[74,75,79–82]

Figure 14(a) shows how the coupling of high laser powers (10 mW at 633 nm) leads to the melting of the aluminum coating in a chemically etched probe. Figure 14(b) shows a metal coating that was ripped off (one laser pulse at 70 µJ at 633 nm).

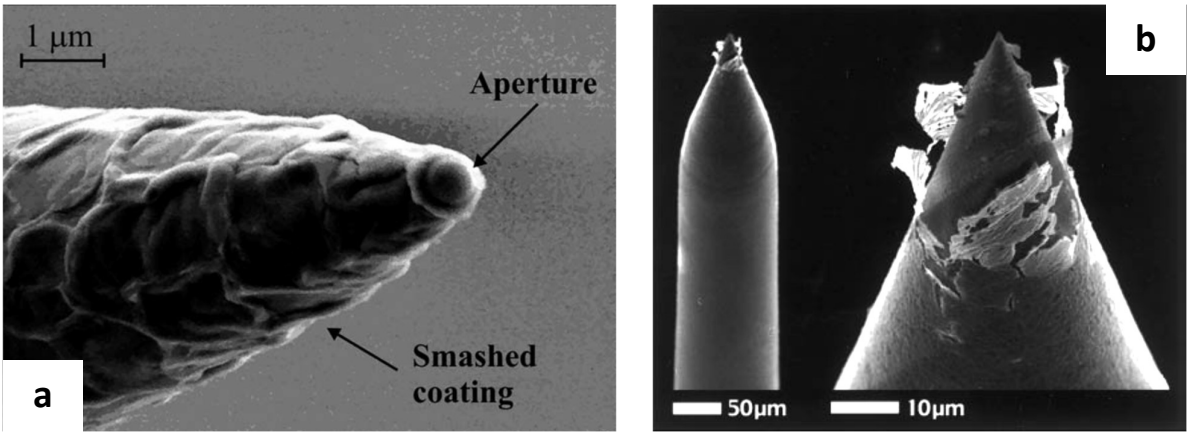

Figure 14 – a) SEM picture of a tube-etched aluminum-coated probe, subject to intense laser irradiation. The thermal damage arises through the melting of the metal film. b) SEM picture of a near-field optical tip after coupling-in overly high laser power. Images taken from refs.[81,82]

In Figure 14(a) the coating is detached from the glass and the surface is completely damaged. Some folds are visible, caused by the local release of the stress due to the different thermal expansion coefficients. In Figure 14(b) the film has been clearly separed from the fiber and distructed near the tip.

SNOM ia a useful tecnhnique for investigation of surfaces, allowing to collect information about position, size and shape of nanoparticles on a surface or embedded in a film. SNOM combined with AFM allows to collect simultaneous optical and topographical maps of the sample.

To give a couple of examples, in Figure 15(a,b) we can see copper nanoparticles, analyzed with SNOM combined with AFM, using an aperture tip.[83] In Figure 15(c) both topografical and optical maps of gold nanoparticles embedded in polyimide film are shown, analyzed with an 80 nm aperture tip, excited by 532 nm laser.[84]

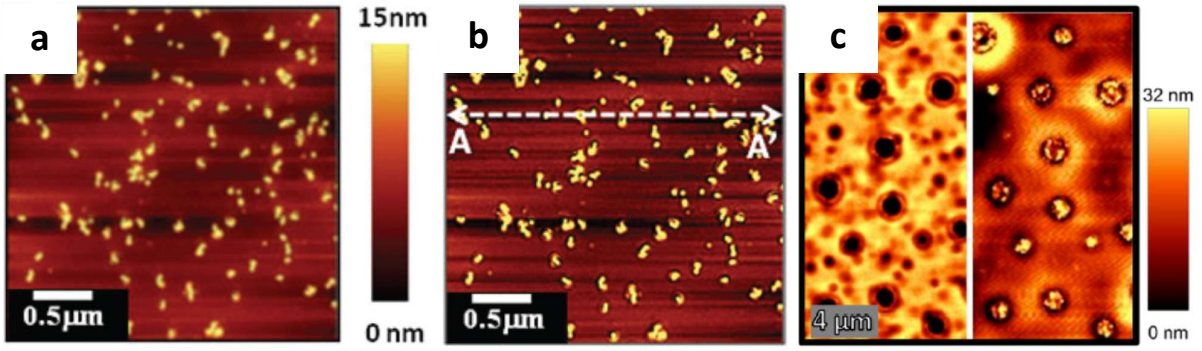

Figure 15 – (a) Topographic AFM and (b) SNOM images obtained simultaneously of Cu-nanoparticles. AFM (left) and SNOM (right) images of Au nanoparticles embedded in polyimide. Images take from refs.[83,84]

Until now I have illustrated probe microscopy techniques suitable for collecting fluorescence, absorption or scattering signals.

As far as Raman spectroscopy is concerned, at present, only a few complex techniques can acquire such signals with nanoscale resolution. The TERS technique is surely one of the most powerful of these. I will briefly introduce this fascinating technique in the next part.

Apertureless SNOM applied to Raman spectroscopy: TERS

Tip Enhanced Raman Spectroscopy (TERS) is a super-resolution imaging technique that brings Raman spectroscopy into nanoscale resolution imaging.[85–89]

TERS imaging is performed with an AFM/Raman system, where a Scanning Probe microscope (SPM) is integrated with a confocal Raman spectrometer through an opto-mechanical coupling. The scanning probe microscope allows for nanoscale imaging, the optical coupling brings the excitation laser to the tip, and the spectrometer analyzes the Raman light providing a spectral image with nanometer scale chemical contrast.

A TERS system is based on a metallic tip (generally made of gold or silver) employed to concentrate the incident light field at the apex. The tip acts as a nano-source of light and local field enhancer, greatly improving the Raman sensitivity (by a factor of 10^3 -10^7) and reducing the probed volume to the "nano" region immediately below the tip. Figure 16 shows a scheme of TERS technique (a) and an example of enhanced spectrum (b). TERS spatial resolution is essentially determined by the tip radius, hence it can reach dimensions smaller than 10 nanometers. The tip converts the near field of higher spatial frequency to far-field so that TERS image with higher spatial resolution is obtained.

By combining point-by-point scanning with simultaneous spectrum acquisition, near-field Raman mappings can be performed with lateral resolution down to ten nanometers or less.

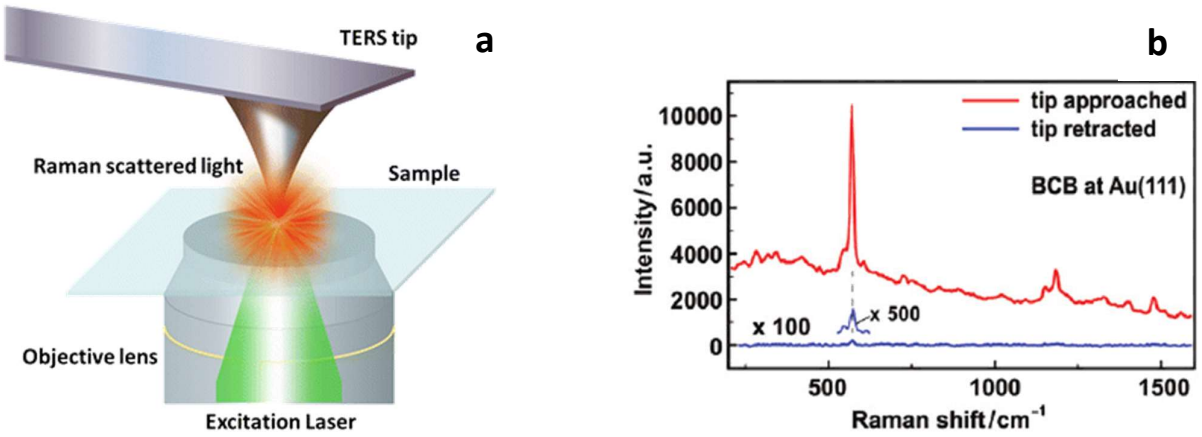

Figure 16 – a) Scheme of classical TERS example. b) Spectra of Brilliant Cresyl Blue taken with (red line) and without (blue line) tip. The magnitude difference is visibly huge. Images taken from refs.[89,90]

Various TERS configurations have been classically used up to now,[6,91–94] and several fabrication techniques has been proposed to produce nanoantennas for this purpose.[91,95,104–109,96–103]

It's very challenging perform a TERS nanoantennas fabrication that is cheap, easily engineerable and with size and morphology of the antenna apex very reproducible. Nowadays, TERS nanoantennas are usually gold tips produced by electrochemical etching [91,95–97], or by attaching plasmonic nanoparticles to standard AFM tips[98–100], or by evaporating gold at the apex of AFM tips[101–103], or milling a finite-size plasmonic antenna using FIB[104,105] Another way to increase probe performances is to reduce the confocal background, adopting a tip-on-aperture approach[106,107], exploiting grating couplers to excite the tip[108], or for example integrating a C-shaped nanogap around the tip of gold pyramid.[109]

My approach in developing a new microscopy probe was based on considering the various critical aspects of the above mentioned techniques. Keeping those limitations in mind was important in order to go beyond these limits in an attempt to develop our new probe. In particular a new SPM probe that can sustain intense E-M fields while maintaining the spatial confinement characteristics offered by a nanoscale aperture. In the next chapters, I will therefore show my experimental work focused to develop this new probe and describe its main innovative properties; innovative properties including the ability to acquire good Raman signals even on a nanoscale scale.

A new paradigm for Scanning Probe Microscopy

Scanning Near-field Optical Microscopy (SNOM), high resolution Raman microscopy and Tip Enhanced Raman Spectroscopy (TERS) are powerful state-of-the-art techniques for surface analysis, that still present some relevant limits. As I mentioned in the previous chapters, some of them are low local power density, poor spatial resolution, not easy to manage by the users or by the image analyses and limited field of applicability.

In order to overcome these significant disadvantages, during my PhD I've developed a new paradigm for SPM called by me: Beam Mediated Microscopy (BeMM). The BeMM approach wants to move towards this techniques for a wider range of applications.

Bead Mediated Microscopy (BeMM)

BeMM exploits the optical proprieties of a dielectric micro bead lens to achieve a nanoscale confinement of light combined with an AFM apparatus to scan samples and obtain optical maps.

The investigation and optimization of this approach to perform high resolution optical microscopy and Raman spectroscopy has been the core topic of my PhD project.

We have seen in the previous chapter that a planar wave that interacts with a lossless dielectric microbead of appropriate refractive index could forms a narrow photonic nanojet, with a minimum beamwidth typically around $\lambda/3$.[21] In this configuration most of the light is wasted because it doesn't hit the bead or hit it at the border where the light beams are not well re-guided towards the nanojet area.

In our setup, we exploit an objective to collect and redirect all the beam towards the central area of the bead. In such way the nanojet is much more intense, but a more accurate alignment is required, Figure 17(a) shows a sketch of the bead illumination in the BeMM optical scheme.

The first step of my work has been the characterization of the optical proprieties of a microscale silica bead embedded in an AFM cantilever (we can see an SEM image in Figure 17(b)), in order to understand them and find the most efficient way to confine light arriving from an objective to achieve an intense nanoscale light source.

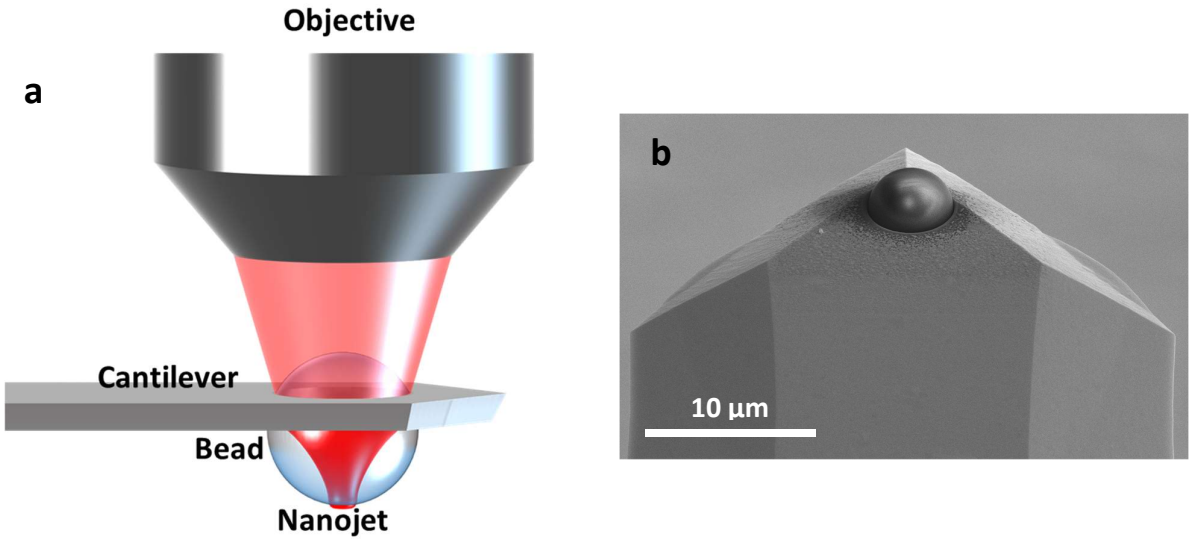

Figure 17 – a) BeMM probe scheme, not in scale. b) SEM image of a BeMM probe. Cantilever is tilted at 52° to better see the bead.

Thanks to the AFM system behind, BeMM probe permits to obtain simultaneously topography and optical maps, the latter with a spatial resolution that is higher than the objective alone. The ability to place and control the bead "in contact" with the sample, pushes up the numerical aperture of the system close to one like a water-immersion objective.[12]

One step ahead for BeMM: SNOM by BeMM. To obtain even higher spatial resolution, I've decided to evolve the BeMM scheme in order to exploit the NF as a nanoscale optical source. The NF source is obtained by covering the lower half of the bead with a metal shield and hereafter by creating a nanohole on it aligned with the nanojet position.

This allows me to obtain a SNOM system that has the remarkable contrast gain of the NF signal generated by the nanohole aperture with a low far field background shielded by the metal coverage.

Moreover, the emission signal that comes back through the nanoaperture can be collected with great efficiency directly by the microbead, which acts as a high NA lens. A sketch of the SNOM-BeMM (S-BEMM) optical probe and its image at SEM are shown in Figure 18.

Thanks to the overall optical strength of the bead, the nanojet of the S-BeMM can support much higher laser intensity that couples with the aperture than in most common techniques. That permits more sensibility, higher scanning speed and the capability to investigate new optical process requiring higher power density such as two-photon effects or Raman scattering.

A lot of work has been done to engineer and optimize the proper nanostructure on the S-BeMM probes to make them acting as a NF source with nanoscale confinement and high power density.

In the following chapters, the employment of advanced nanofabrication techniques for this purpose will be described.

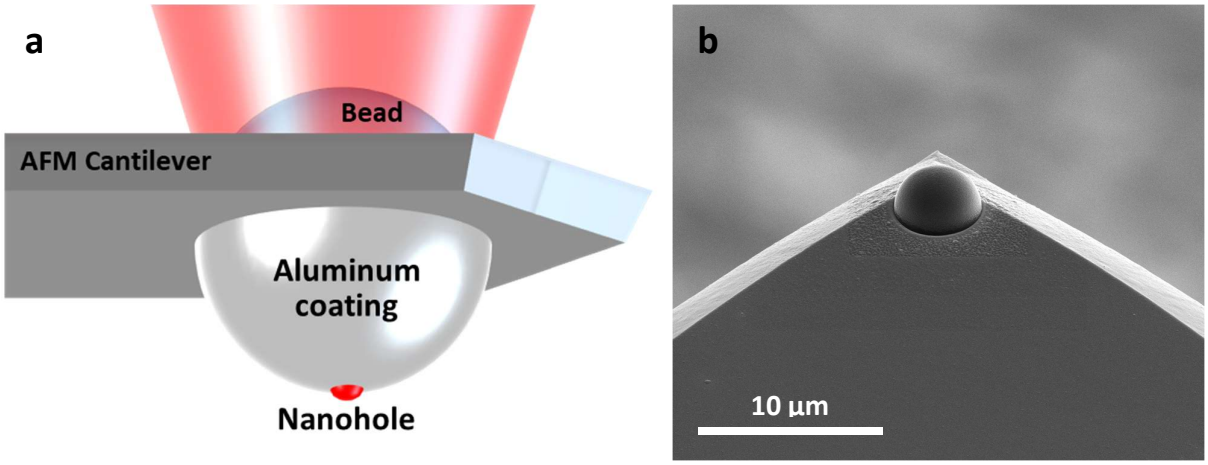

Figure 18 – a) S-BeMM probe scheme, not in scale. b) SEM image of a S-BeMM probe. Cantilever is tilted at 52° to better see the bead.

As the standard SNOM technique, S-BeMM is versatile, because the probe can be used as excitation source or collection tool, but also as both of them at the same time. This opportunity makes S-BeMM suitable not only for transparent samples, but also for opaque ones, increasing greatly its applicability.

Experimental setup

The experimental setup I used for my experiments is a commercial one from WiTec company. The WITec 300 alpha is an integrated optical system that combines an inverted and a direct microscope with a scanning probe tool. General scheme is shown in Figure 19

This instrument allows confocal Raman imaging and mapping in combination with AFM analysis for high-resolution nanoscale chemical and surface characterization. Moreover, a transmission collection system under the sample holder permits SNOM optical imaging with nanoscale resolution.

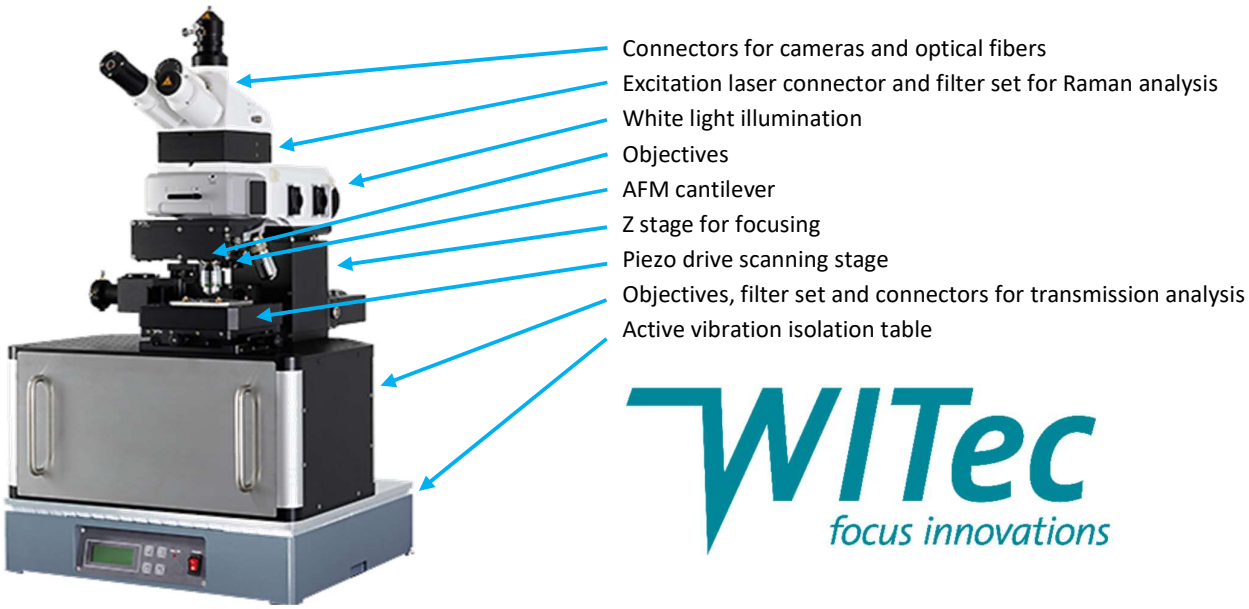

Figure 19 – Witec 300 alpha experimental system

Optical setup

I arranged the optical setup to take measurements in three different ways: reflection mode, transmission mode, or the combination of both optical modes

Reflection configuration

In reflection configuration, both the excitation process and the collection of the optical signal take place on the same side of the sample, the upper side in our case. The excitation laser (Research Electro-Optics Helium-Neon 632.8 nm, 35 mW) enters in the optical system

through a rear port (equipped with an FC/PC connector and collimation optics) placed between the lens and a tube lens.

The laser comes from a single mode optical fiber (Thorlabs P3-630A-FC-1) and is collimated by a lens. It's reflected by a dichroic filter (Razor edge LPF 632.8 nm) and focalized by an objective (Olympus LMPLFLN 50x, NA 0.5) on the BeMM probe.

The sample emission signal is collected by the same objective and passes through the dichroic filter before reaching the detectors area. Detection can be performed either by collecting the image through a CMOS camera (Imaging Source DFK 42AUC03) or through the optical spectroscopy channel. In order to detect the spectral components, the light is focalized by the tube lens into a large multi-mode optical fiber (core diameter 100 µm), and the fiber output is detected by an Ultra-High Throughput Spectrometer (Witec UHTS 300) composed by a monochromator with a 600 lines/mm grating (resolution 0.09 nm) and a high efficiency EM-CCD array (Andor Newton DU970N-BV). Figure 20 shows a sketch of the reflection configuration setup with the two detection lines, prepared and used for the experiments.

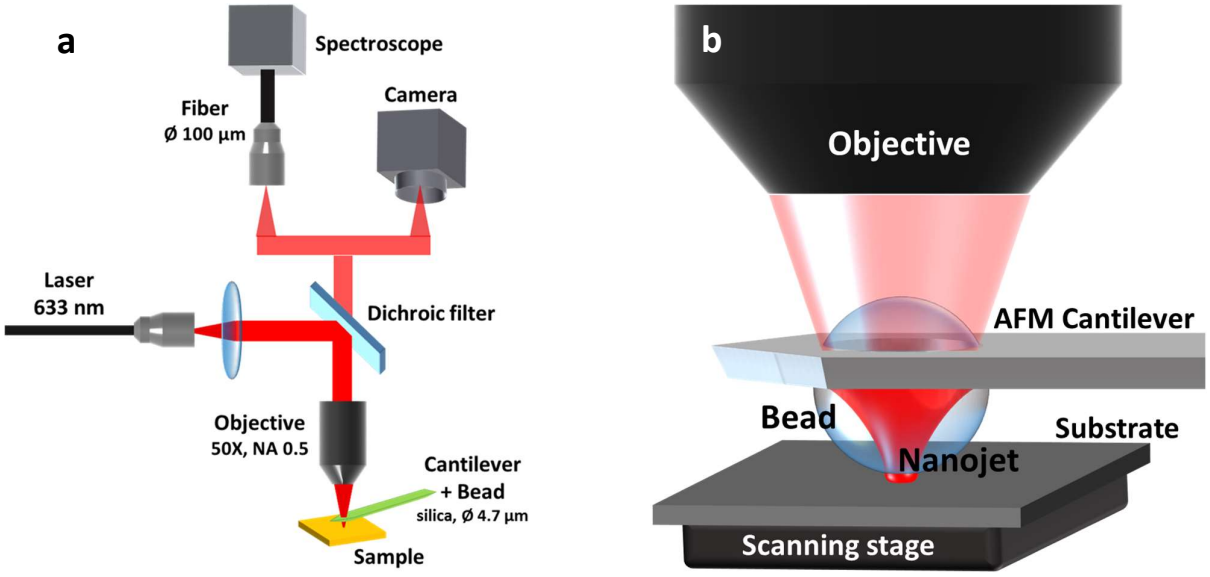

Figure 20 – a) Sketch of the experimental setup used in reflection configuration, with the two channels of detection. b) Detailed sketch on the BeMM probe system.

BeMM probe is mounted on the AFM arm and positioned under the objective in a specific position, opportunely identified according to experimental measurements showed in the following chapters. In such position the nanojet is created perfectly over the sample and the bead is able to recollect the scattered or emitted light that comes back from the sample surface.

Transmission configuration

The setup used for the "transmission mode" measure has the same excitation part of the "reflection mode" configuration, see Figure 20, but with a different, separated, collecting scheme under the sample. Under the scanning stage an objective (Olympus LUCPLFLN60X, NA 0.7) is placed to collect the signal emitted from the sample. The objective is mounted on a three-axis motorized translator that allows a precise correct positioning of the collection point. After a filter stage made with a notch and a long lass filter, the collected rays are coupled again by a lens tube and an optical fiber to the Witec UHTS 300 monochromator, as the "reflection mode" optical scheme. The sample could be observed by a motorized flip-flop mirror right after the tube lens. Figure 21 shows a sketch of transmission mode setup with the components for collecting the optical signals and observing the sample.

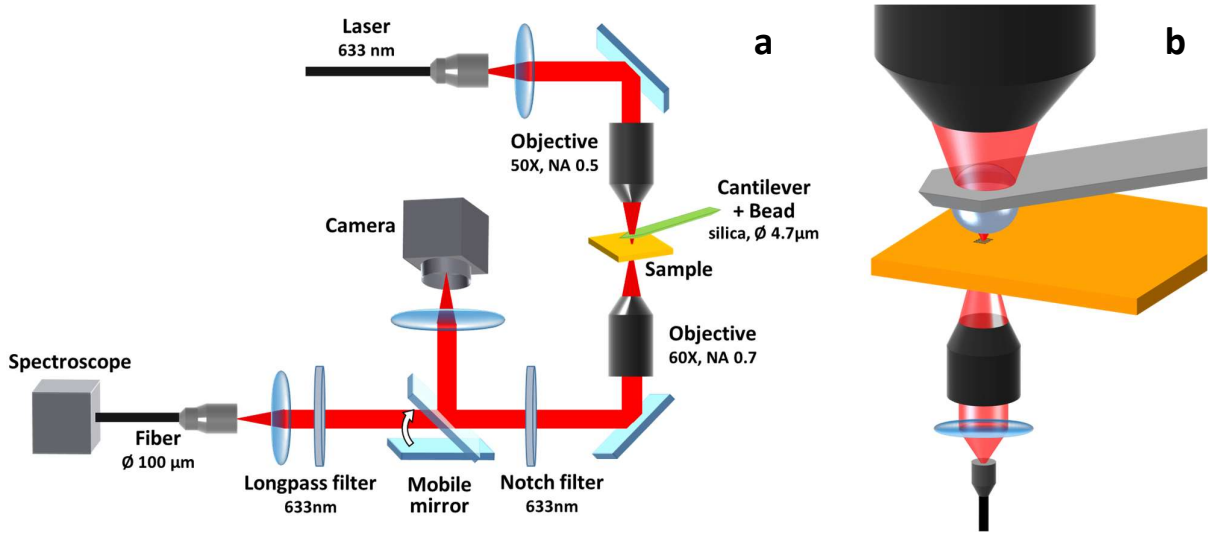

Figure 21 – a) Scheme of the experimental setup used in transmission configuration. b) Zoom on the BeMM probe system and the collection system.

The transmission mode has the advantage of avoiding the double use of the bead, illumination and collection, with a strong increase in collected light and greater the overall efficiency. Unfortunately, this scheme is limited to transparent samples only.

AFM setup

Witec AFM system is equipped with a motorized arm mounted under the upper objective. On this arm the cantilever can be magnetically attached and moved in x,y,z directions to align the cantilever with the AFM laser. The upper objective provides a direct view of both sample and cantilever for tip positioning.

During the approach and the scan, the cantilever deflection is monitored through a laser beam-deflection system. The AFM laser (405 nm low power diode) is aimed to and reflected back by the cantilever. The back reflected rays are collected by a Position-Sensitive Detector (PSD) consisting of four photodiodes. The equilibrium condition is when the laser is reflected at the center of the four photodiodes array, any variations in the cantilever bending causes variation on the PSD signals. By monitoring that signals is possible to control the feedback loop and maintain the gap between sample and tip constant.

The preliminary step of a scan is the tip-sample approach. The probe approaches the sample from above until the tip interacts with the surface and the feedback system reads a signal variation equal to the user defined set point value, then it stops and it's ready for scanning. By modifying the set point value, the user can define how "gentle" or "aggressive" the interaction between the probe and the sample is.

The system includes a piezoelectrically driven 3-axis scanning stage with a scan range of 200 µm along X and Y directions and 20 µm along the vertical direction, Z.

With BeMM probes, I scanned the samples surfaces in soft contact mode, where the probe is in continuous contact with the sample during the scan. I operated in constant gap mode, so, thanks to the deflection feedback signal, the system moves the piezo stage along Z to maintain the probe-sample distance constant. In this case the surface topography is reconstructed by recording the stage x,y,z coordinates.

BeMM probe and test samples fabrication

BeMM probe fabrication

In all fields of probe microscopy, quality and efficiency of the probe are fundamental elements for successful measurements.

BeMM probe fabrication process started from a standard tipless AFM cantilever, I used Budget Sensors All-In-One-Al-TL cantilever,[110] in which I drilled a hole and embedded a microbead.

To realize a hole for the bead integration, I used Focused Ion Beam (FIB) (Tomahawk ion column on FEI Helios NanoLab DualBeam 650), patterning a circular geometry with a diameter of 4.7 microns. Then I checked its shape and dimension by Scanning Electron Microscope (SEM) (Elsta monochromated Schottky FESEM on FEI Helios NanoLab DualBeam 650). See Figure 22 as typical SEM image of the hollow cantilever fabricated by FIB.

The hole is made close to the cantilever apex with a diameter that is a just few tens of micrometers smaller than bead diameter. In this way the bead will not pass through the hole and the main part of the bead will stick out from the lower surface of the cantilever. This process is quite important in order to make sure that only the lower portion of the bead will be in touch with the sample during the mapping, avoiding any accidental contact of the cantilever apex with the sample surface.

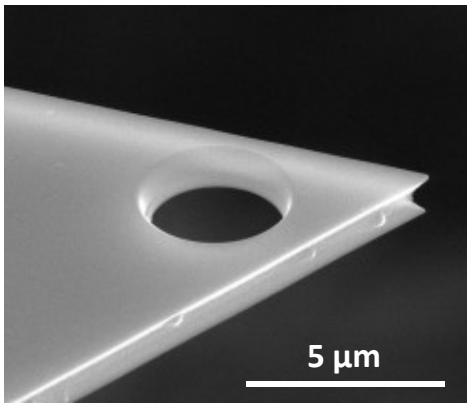

Figure 22 – SEM image of the hollow cantilever fabricated by FIB.

Then the cantilever is mounted on a proper ferromagnetic washer using a cyanoacrylate glue, in order to mount it on the magnetic holder for AFM probes.

The bead setting process is reasonably reliable and fast and is based on picking the bead up simply by pressing it with the holes in the cantilever. A bead drop casting process is

carried on when few drops of aqueous solution with silica beads (Ø 4.9 µm) are dropped onto a transparent microscope glass slide and then left to dry. Figure 23 shows the scheme of the bead "fishing" process.

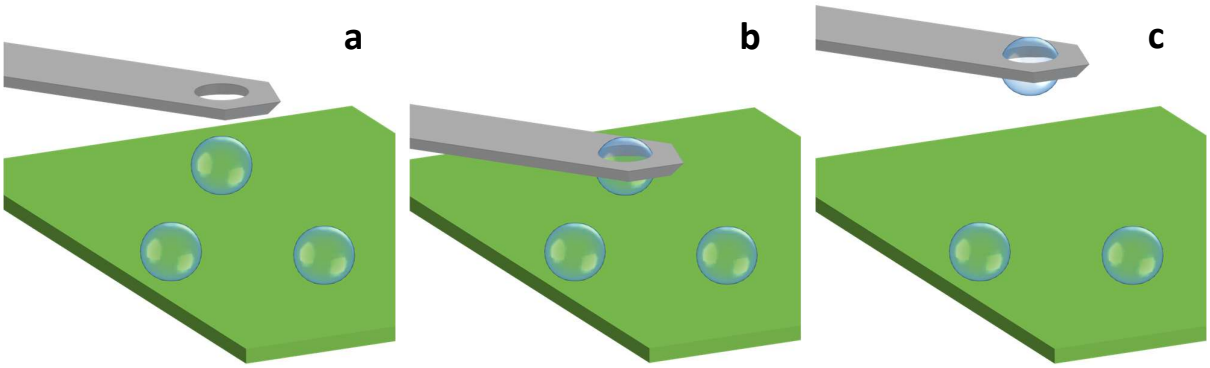

Figure 23 - Scheme of BeMM probe fabrication: a) Hollow cantilever approaches to a bead dispersed onto a substrate. b) By pushing down the cantilever, the bead fits inside the hole. c) Raising back the cantilever, the bead is picked up.

Exploiting the vision system from below [Figure 21(a)], it is possible to localize an isolated single bead and vertically align the cantilever hole with it. Then, by lowering the cantilever on the slide surface, and, once in contact, pushing more slightly down, the cantilever will fit the bead into the hole. After the cantilever is raised back, the bead remains embedded due to electro-mechanical bonding.

Unfortunately, the drying process of the bead solution leave the bead surface covered by the dried buffer medium. Therefore the cantilever with bead have to be immersed in pure acetone for 5 minutes in order to dissolve the unwanted coating. Figure 24 shows the cleaning effect.

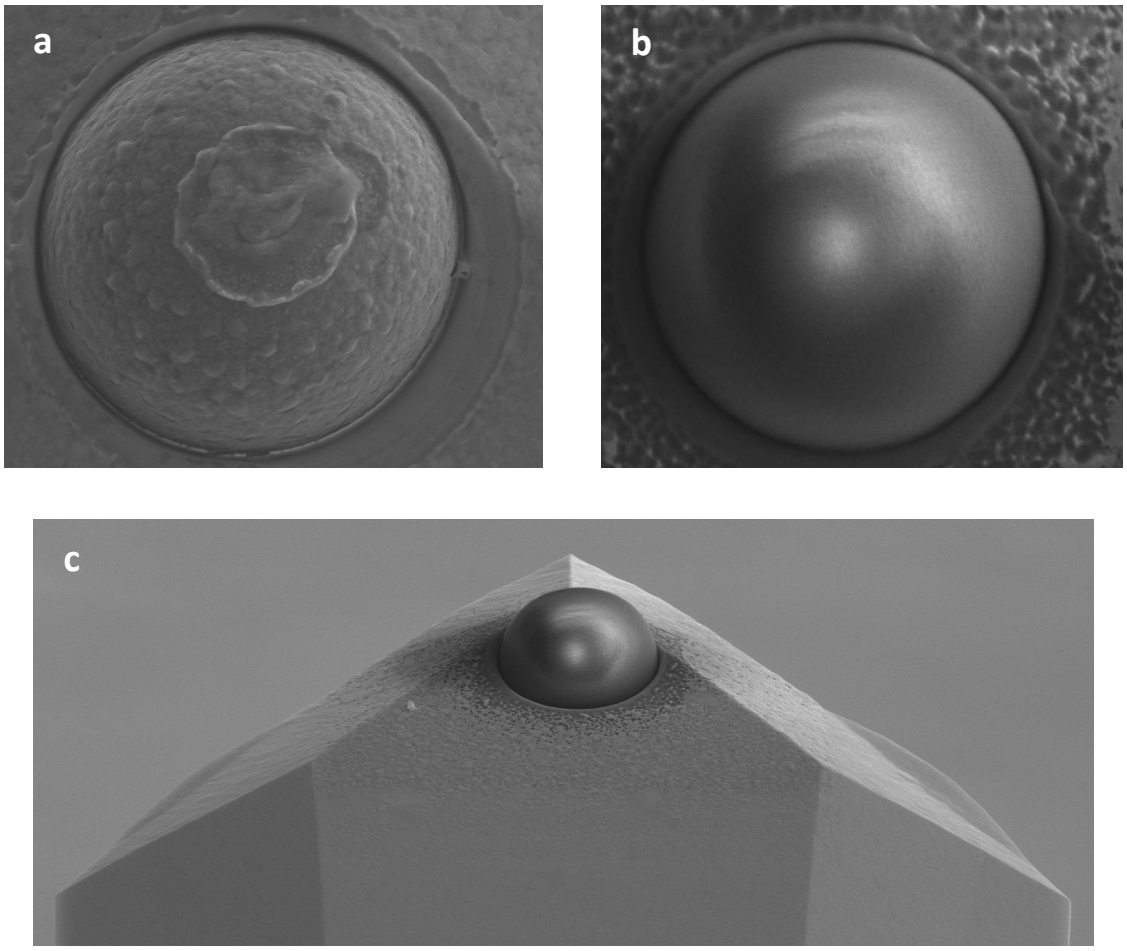

Figure 24 - SEM images of beads embedded in cantilever before and after the cleaning process. a) Uncleaned bead covered with 20 nm of gold for imaging purpose. The unwanted deposit coming from the bead-substrate contact point is quite evident. b) Bead cleaned after the acetone dipping process. c) Zoom out on the cantilever tip with the bead element.

This probe is suitable to be used for BeMM and is the basic structure for its developments towards near field microscopy as I will highlight in the following chapters.

S-BeMM probe fabrication

Stepping forward, to evolve the BeMM probe to an optical near field source, some important fabrication steps have been implemented. Firstly the lower side of the bead is covered with 50 nanometers of metal. Then a hole of a few tens of nanometers is made in the nanojet region that turns out perfectly aligned with the position of bead-sample contact point. In this NF probe, the metal coating act as “shield” for the incoming excitation light and so the hole become a small and focalized near field source with high contrast with the background illumination.

Coating

The appropriate coating has a strong influence on the performance and lifetime of the S-BeMM probe. Although its main purpose is to shield the light coupled to the bead, I evaluated the aspects of wear and resistance under laser illumination. Based on their optical and mechanical properties, I selected the following materials: gold, titanium, chrome and aluminum. For each element I made coating of 50 nm and observed the bead before and after a 40-minutes scan in contact mode over an area of 10 µm to 10 µm. In gold case I added below 5 nm of titanium adhesion layer to increase the gold-glass adhesion.

Although the first three metals have similar transmittance, gold is the only one that could give a high local field enhancement due to plasmonic resonances, but has been found to be poorly resistant to wear due to its low hardness (see Figure 25(a)). On the contrary, titanium, chromium and aluminum have much higher hardness, in fact they lasted mechanically stable without being ruined.

From the point of view of the optical shading, such thin thicknesses of material require more attention. When the nanohole made is in the order of 100 nanometers, the evanescent wave intensity becomes comparable to the intensity of the light transmitted through the metal layer. This similar intensity causes the overlapping of the two components and, consequently, worsens the spatial resolution. For these reasons, I chose aluminum as coating element, because for radiation with λ of 633 nm, transmissivity of aluminum is one order of magnitude lower than gold, titanium and chromium[111]; while it proved to maintain excellent mechanical proprieties (see Figure 25(b)).

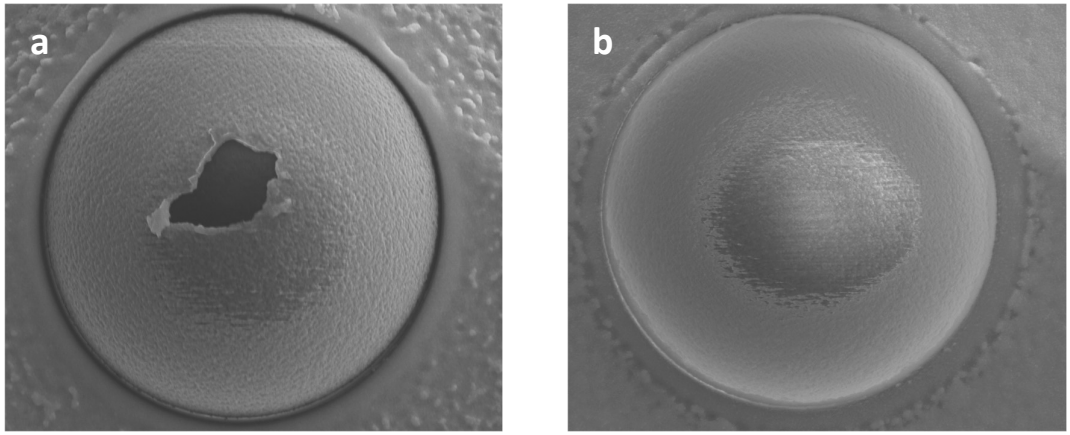

Figure 25 – SEM images of beads covered with different metal layers, after a 40-minutes scan, area 10 µm x 10 µm. a) Bead covered with 5 nm of titanium and 50 nm of gold. b) Bead covered with 50 nm of aluminum. The shadow areas with a diameter in order of 2 µm in the middle of the images are an artefacts effect due to the slow electric discharge of the electrons during the acquisitions.

Nanohole

The most critical aspect of S-BeMM probe fabrication is the alignment between the nanojet, the nanohole and the bead-sample contact point. Since the near field is confined within few tens of nanometers far from the aperture, any misalignment between the NF aperture and the bead-sample contact point reduces the intensity of interacting near field. In the same way, if the nanojet does not coincide with the position of the opening, the light coupled on it is lower, reducing the overall efficiency.

The path towards the alignment improvement passed through different trials and in the end I chose the following way.

First of all, I acquired an SEM image of the lower part of the metal covered bead [Figure 26 (a)]. Then I cleaned carefully a microscope glass slide and I coated it with carbon through sputtering deposition, reaching a surface layer of some tens of nanometers. After that, I approached on this substrate with the metal covered bead and scanned the surface to mark the contact point with carbon in a visible way under SEM. Afterwards, I made a second SEM image [Figure 26 (b)] and compared the two images, identifying the area that became slightly different due to the carbon presence.

A good alignment between electron beam and ion beam has to be done to create the hole in the position as accurately as possible. So I made the nanohole directly in the center of the marked area [Figure 26 (c)]. This procedure seems to be enough reproducible and permitted me to improve the alignments I talked above. Figure 26 shows the steps of this contact point localization and of the subsequent hole fabrication.

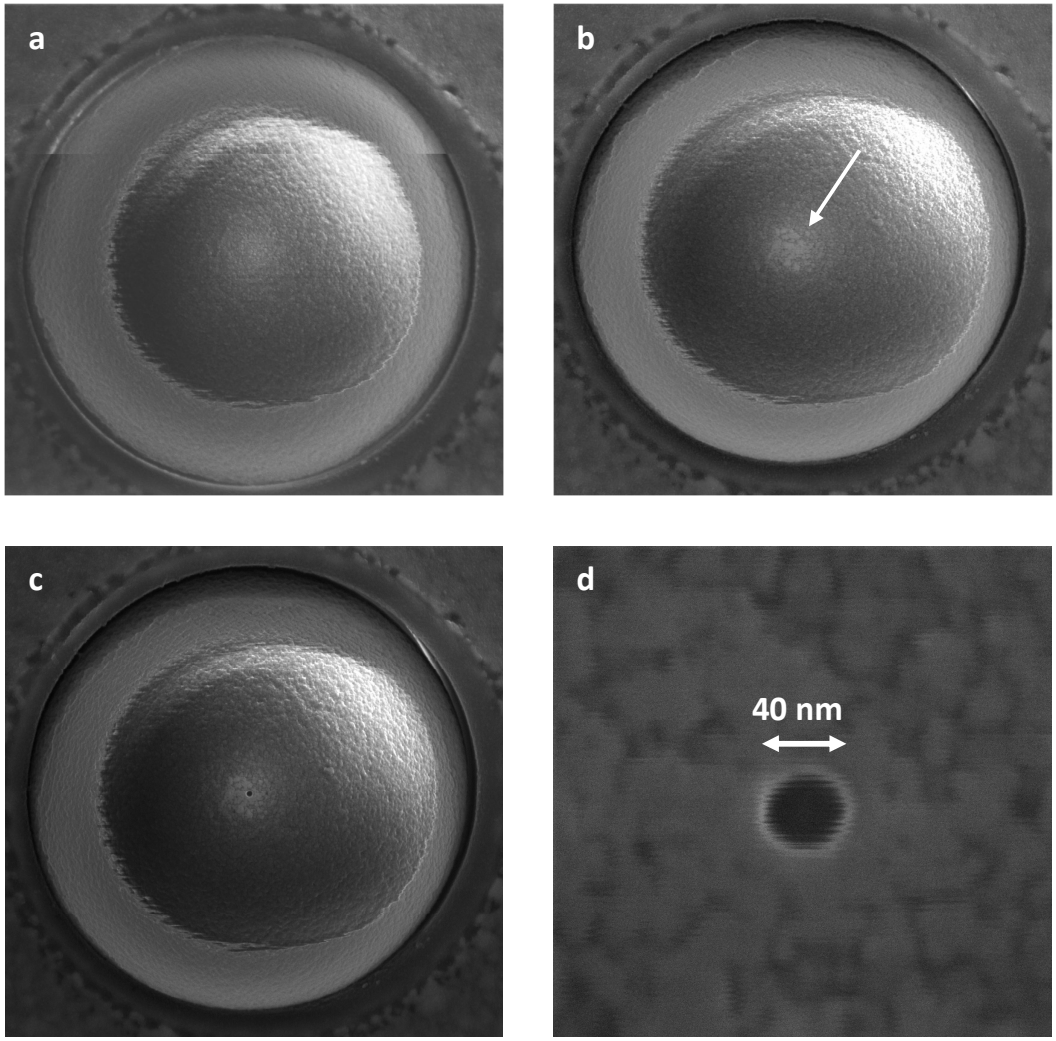

Figure 26 – a) SEM image of the bead covered with metal. b) SEM image of the covered bead after the carbon marking. The marked area, indicated by the white arrow, is brighter than the surrounding zone. c) SEM image of the bead with a 40 nm nanohole made in the center of the marked area. d) Zoom on the nanohole. The shadow areas with a diameter in order of 3.5 µm in the middle of the images are an artefact effect due to the slow electric discharge of the electrons during the acquisitions.

Test samples for BeMM and S-BeMM

In order to characterize the probes manufactured for S-BeMM and evaluate their characteristics and capabilities for near field microscopy, I made samples with specific features. I wanted to produce samples that were basically flat, with well know spatial elements of nanometric dimensions.

After some trials and tests of different materials, particles and fabrication processes, I selected the following kinds of samples.

Scattering samples

Samples for scattering measurements were prepared both with transparent substrates and with opaque ones. I washed glass coverslips and silicon samples with soap for optical cleaning, acetone, isopropanol and deionized water. Then these substrates were dried with nitrogen and I performed an additional oxygen plasma cleaning as last step.

I evaporated different metals on different substrates, like gold and chromium, and I tried different thicknesses, from 15 to 50 nanometers. All these films were deposited via electron beam deposition in high vacuum, with a Kenosistek KE500ET equipped with a Ferrotec EV-M6 source.

These samples were then patterned by FIB to obtain some well-defined areas with an exposed substrate surrounded by pure metal. In these way the optical properties differences lead to distinct optical signal from the various areas.

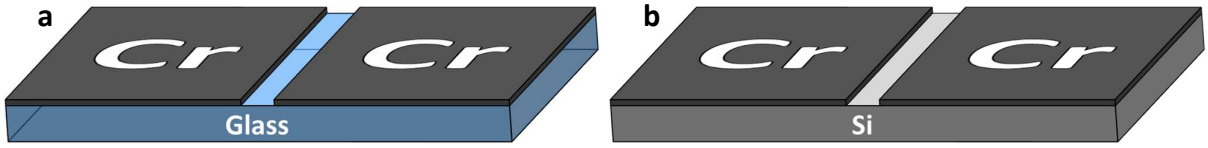

Figure 27 – Sample schemes for scattering measurements: a) Glass substrate covered with 15 nm of chromium and patterned by FIB. b) Silicon substrate covered with 15 nm of chromium and patterned by FIB.

I mainly patterned some areas with very sharp borders for the knife-edge test (see next chapter) and also narrow stripes (30 nm wide), in order to have structures whose dimensions are well below to the expected system PSF. In this way, I could perform mathematical operations on the intensity profiles and obtain information about the probe PSF.

Fluorescent samples

Initially I prepared and analyzed a fluorescent sample, because a fluorescence signal is spectrally much easier to identify and it's much more intense than a Raman signal, thus the analysis are sensibly simpler.

To prepare a randomly patterned sample with nanostructured fluorescent elements, I added a solution of 40 nm polystyrene nanobeads loaded with dark red fluorescent dyes (emission peak at 680 nm) in a Poly Methyl MethAcrylate (PMMA) A4 anisole solution. After having found the proper viscosity and particles concentration, this blend has been spin coated onto an optically cleaned glass coverslip at 4000 rpm; the final thickness was around 200 nm. A thinner layer would have been more desirable to limit the nanobeads distribution along the Z axis; beads too far from the surface don't manage to interact with the localized near field of S-BeMM probe. Anyway it was the thinnest I managed to obtain.

The randomly distributed beads show a fluorescence pattern with nanoscale features.

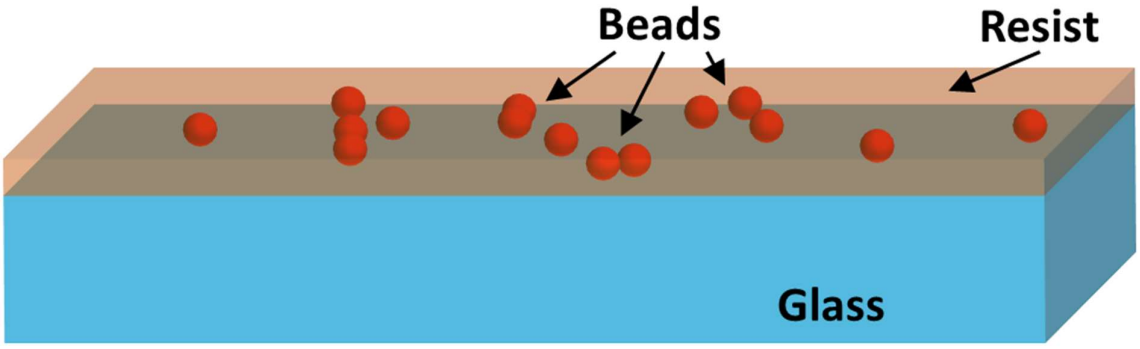

Figure 28 – Sketch of the fluorescent sample structure

Raman samples

In order to expand the application range of BeMM and S-BeMM to Raman spectroscopy, I produce several kinds of Raman samples with nanoscale features, which are much more challenging to handle, because the optical signal is extremely low.

I already discussed the preparation of some of them in the chapter "Scattering samples", but in this case I need to add some details. For the Raman preliminary analysis I used only clean plain silicon substrates. Silicon has a very clear and well known Raman peak at a wavelength shift of 521cm^{-1}. I covered silicon with a thin metal layer (15 nm), trying both gold and chromium. Maps collected on gold covered samples were distorted respect to the real patterns, while this variation there wasn't on chromium samples. This effect was caused by surface plasmons in gold borders, which created areas of strong and localized field enhancement and consequently altered the collected Raman signal. The thin thickness has been chosen because a thicker shielding layer moves the NF source far from the substrate making its interaction not optimal and not very intense.

Moreover, I considered the Carbon NanoTubes (CNTs) as a nano source of Raman signal. Raman scattering is one of the main characterization techniques for CNTs, because they show specific peaks patterns related to phonons, which can supply information about their geometry, electrical properties, defects, aggregation state and interaction with the environment.[52,112–118]

Vibrating modes of a CNT are the fingerprints of its specific characteristics and can basically be sorted in two families: high energy modes, which are divided in D-band (roughly around 1350 cm^{-1}) and G-band modes (roughly around 1600 cm^{-1}), and low-energy Radial Breathing Modes (RBM), which usually are below 500 cm^{-1} and are much less intense.

All this modes are sensible to the properties previously described, in addiction high-energy modes "feel" the bending states and in general strain and deformation,[119,120] while RBMs are associated with the symmetric movement of carbon atoms in the radial direction and are linked to dimension and chirality.[121]

All this characteristics act on the Raman peaks intensity, frequency shift, splitting and in some cases on the emergence of new peaks. This influence allows us to characterize CNTs by the analysis of their Raman Spectra.

In Figure 29 are shown a scheme of the Raman spectrum of CNTs, where we can see the energy bands introduced above, and a typical chart for the estimation of CNTs diameter from the RBMs shift.

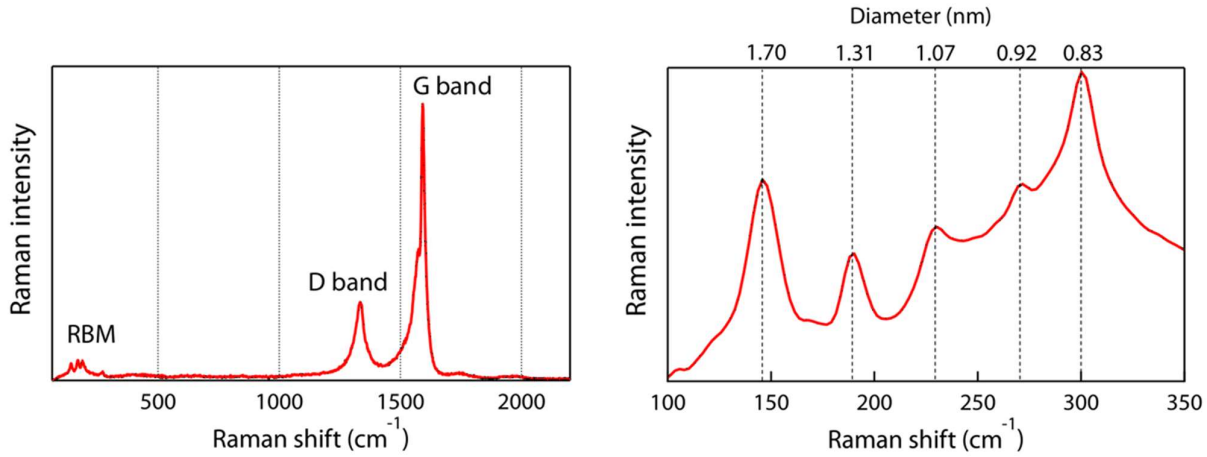

Figure 29 – Left: CNT Raman peaks. Right: relationship between RBM peak and CNT diameter. Images taken from ref.[122]

In addition to attracting optical properties, CNTs have also a geometry that is interesting to be analyzed with a scanning probe. A single CNT has a length of some micrometers and a diameters of few nanometers, making them perfect test samples to fully explore the properties of a system like S-BeMM.

I took a concentrated solution of Single Walled CNTs (SWCNTs) in N-Methyl-2-Pyrrolidone (NMP) and I made several dilutions in different solvents; then I spinned these solutions onto glass coverslips previously cleaned for optical analysis. Analyzing the substrates though Scanning Electron Microscope (SEM), I found the best solution and the best covering process: I prepared a solution of SWCNTs diluted, primarily, in NMP and then in acetone. The solution was finally spinned for 60 seconds at 6000 rpm, onto a standard glass coverslip cleaned for optical analysis. Figure 30 shows an SEM image of an area of the CNTs sample surface.

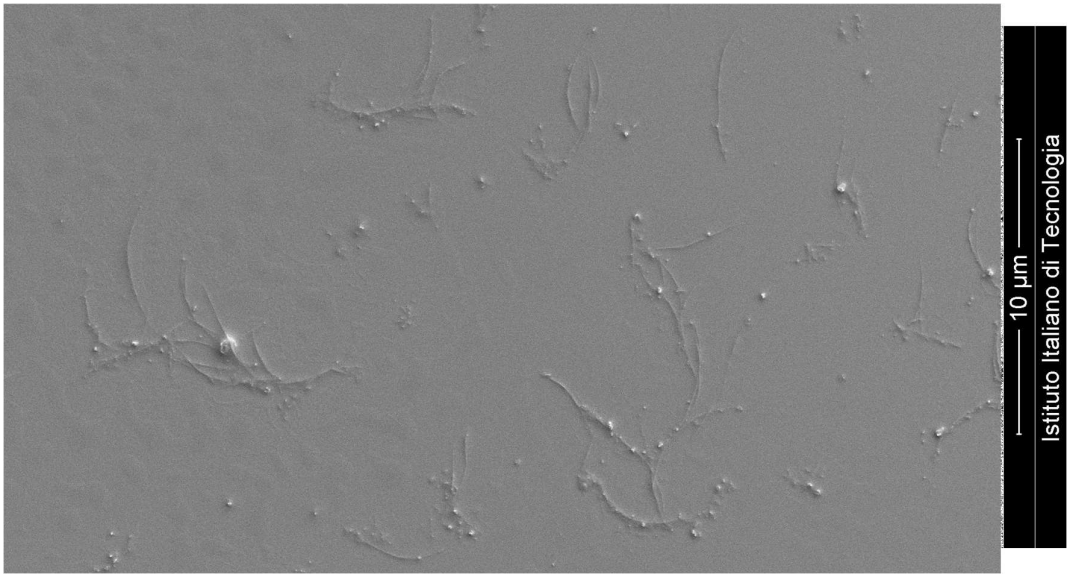

Figure 30 – SEM image of SWCNTs solution (in NMP and acetone) spinned for 60 seconds at 6000 rpm onto a glass coverslip.

BeMM and S-BeMM, characterization and experimental tests

Characterization techniques for spatial resolution

For any microscopy system in general as well as for SPM in particular, the characterization of its performances is very important. Hence, I focused part of my lab activity to characterize optical and mechanical properties of BeMM probes that I'm proposing.

Spatial resolution is one of the most fundamental parameters that has to be evaluate correctly. I would define resolution as the minimum distance at which two point sources can be distinguished.[7,123,124] In a perfect classical imaging system part of the radiant energy emanating from a point source in the object plane would be concentrated at a point in the image plane, the ideal image point. Practically, many factors occur to cause the broadening of the ideal image point. The radiation intensity distribution of a point source is larger and is defined the Point Spread Function (PSF) of the system.

The intensity distribution of a single source has a bright central region, called Airy disk, and a series of low intensity concentric rings around. Its 2D profile can be described by the equation $J = I_0\, sin^2 x/x^2$.[123,124] The distance between the maximum intensity and the first minimum is defined as the radius of the central Airy disk and in optical microscopy is equal to $r = 0.61\, \lambda/NA$.[8,125]

Following Rayleigh criterion, two point sources are regarded as just resolved when the zero-order diffraction maximum of one diffraction pattern coincides with the first minimum of the other.[7] Thus, PSF is directly related to the resolving power of the optical system: by collecting it, we can measure the central disk radius of the Airy pattern obtaining the spatial resolution according to Rayleigh criterion. Furthermore, NA can be calculated by this. The smaller the PSF, the higher the spatial resolution and the NA.

A graphical explanation of Rayleigh criterion is shown in Figure 31, with a two equal sources distribution and its equation.

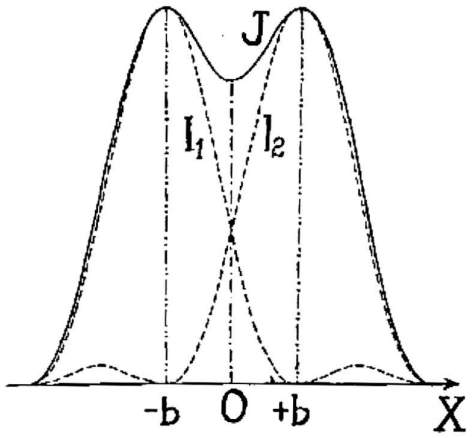

$$J = I_{1,2}\left\{\frac{sin^2(x-b)}{(x-b)^2} + \frac{sin^2(x+b)}{(x+b)^2}\right\}$$

Figure 31 – Left: diagram to show the application of the Rayleigh criterion on two emitters. I_1 and I_2 are the intensity curves, J is the composite curve, x is the spatial parameter in terms of which the distribution is described, and 2b is the radius of the Airy disk, which Rayleigh propose as spatial resolution limit. Right: equation of the distribution on the left, where $I_{1,2}$ is equal to I_1 and I_2. Image and equation taken from ref.[123]

In his influential article (ref.[7], pg. 266) Rayleigh calculated that, for two emitters at minimum resolvable distance, the intensity of the optical signal at the midpoint between the two and the maximum of one of the two are in a ratio of 0.81. Hence, it's also possible to obtain the spatial resolution parameter finding the distance between two emitters that brings this intensity ratio. Regular gratings with known periods are typically used for this purpose.[126]

It is possible to perform an alternative calculation of the single emitter distribution shape, [127] approximating the central Airy disk with a Gaussian profile, ignoring the relatively small outer rings of the Airy pattern, thanks to the fact that the central Airy disk contains the 84% of the intensity. In good approximation, the two curves are practically overimposable.[128] In practice, I used this approximation for fitting my PSFs. Gaussian curve minimums are not at finite abscissa values, so I had to calculate the Airy radius from another parameter, the Full Width Half Maximum (FWHM). From the normalized Airy pattern function, we can easily calculate that the value at which we have an intensity of 0.5 is ≈ 1.39, for an Airy disk radius of π. Hence, the relation between the FWHM and the Airy disk radius r is $FWHM = [(2 \cdot 1.392)/\pi]\, r \approx 0.89\, r$. It follows that, according to the Rayleigh criterion, the spatial resolution is around 1.12 times the FWHM of the Airy disk, i.e. the PSF.

In Figure 32 the unit point source is shown as an arrow of unit length standing on the object plane and the PSF as a "bell" distribution on the image plane. For most optical systems, the PSF possesses rotational symmetry on x,y axis.

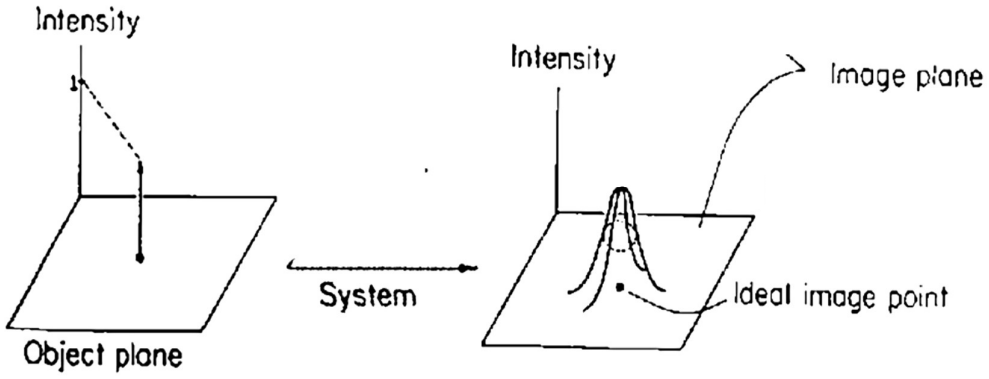

Figure 32 – Unit intensity point source and the relative PSF imaged by an isotropic system. Images from ref.[129]

A linear system follows the superposition principle of linear imaging; hence, the total image of all point sources is the sum of all corresponding PSFs over the image plane. Moreover, if the intensity of a unit point source is multiplied by some constant, then the corresponding PSF will be multiplied by the same constant to obtain the image of the point source of non-unit intensity.

This two properties lead to the conclusion that, if the input consists of a field of point sources of different intensity (in practical cases a continuous two dimensional object can be considered as an aggregate of an infinite points), the output of the total image is the sum of all the point images. Hence, the final image becomes the convolution between the real points and the point spread function, each multiplied by an appropriate constant to take account of the intensity of the corresponding point source.[129] Thus, from a knowledge of the system point spread-function and of the output intensity distribution in the image the real input intensity distribution in the object can be determined.

Convolution is the mathematical operation of multiplying each point in the object intensity distribution by the PSF, obtaining the "broadened" image provided by the system. To know the given system convolution effect, PSF should be measured by using a point source.

Direct measurement of PSF, however, is difficult for two experimental reasons. First, ideally, the source should be a "numerically" single point, obviously, this is not physically possible and so we approach this concept using a source that is much smaller than the PSF of the optical system. A so tiny emission source means a very low intensity. Second, measurement of the resulting intensity distribution in the image plane requires scanning exactly through the center of the distribution, which causes alignment difficulties. These experimental problems can be overcome calculating the PSF by the measurement of other transfer characteristic of the system, for example the Line Spread Function (LSF).[129]

The LSF represents the radiation intensity distribution in the image of an infinitely narrow and infinitely long line source of unit intensity. In Figure 33 the unit line source is shown as an infinite line of arrows of unit length standing on the object plane, and the LSF as a "dune" distribution on the image plane.

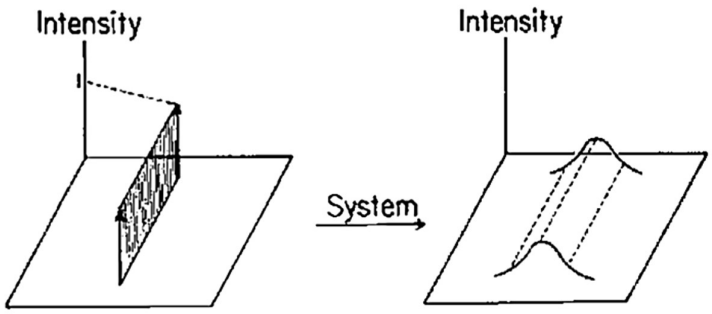

Figure 33 – Unit intensity line source and the relative line spread-function imaged by an isotropic system. Images taken from ref.[129]

LSF is measured by approximating a line source with a slit which is narrow and long relative to the size of the point spread-function, and by scanning the resulting output (the slit image) with a narrow slit. This experimental technic eliminates both difficulties associated with the direct measurement of the point spread-function.

Determining the point spread-function from the measured line spread-function, however, is no simple matter in general. This is due to the fact that the line spread-function is a one-dimensional function obtained from a rectilinear scan of a one-dimensional intensity distribution, whereas the point spread-function is two-dimensional. This can be explained by noting the relationship between the two functions. It can be shown mathematically that the direct measurement of the line spread-function described above is equivalent to scanning the point spread-function with a slit which is narrow and long relative to the size of the point spread-function.[129]

If the imaging system is isotropic, PSF is rotationally symmetric and the shape of the LSF is independent of the orientation of the line source in the object plane. Thus, if the system is isotropic, one measurement of the line spread-function suffices for the calculation of the point spread-function.

To summarize, LSF serves as an experimentally accurate tool for determining the PSF, which is a system transfer characteristic for the most general case of two-dimensional radiation intensity distributions in the object plane.

If the system is linear, an input consisting of a field of line sources of arbitrary intensity will result in an output which is the sum of the corresponding line spread-functions, each multiplied by an appropriate intensity factor. If the input is a continuous object over which

the radiation intensity varies in one dimension only, such as a straight-edge or a bar pattern, the object can be considered as an aggregate of an infinite number of line sources of different intensities. The corresponding output is calculated by multiplying each line source in the object intensity distribution by the system line spread-function and summing over the entire object distribution. Therefore, LSF is a transfer characteristic of linear, isoplanatic imaging systems for the special case of one-dimensional inputs. LSF provides sufficient information for the evaluation of PSF in general. LSF leads to a simplification of the overall problem only in the case of one dimensional inputs. In the study of isotropic systems the orientation of the slit relative to the system can be ignored.

There are few ways to evaluate PSF from LSF. The one that I consider most accurate is called "knife-edge method" and involves the scan on a sharp edge.[130] The differentiation of the intensity profile extracted perpendicularly to the edge provides the LSF, which is basically the one dimension equivalent of the PSF. That procedure often involves a Fourier transform to the PSF, and is largely applied especially in high resolution cameras characterization.

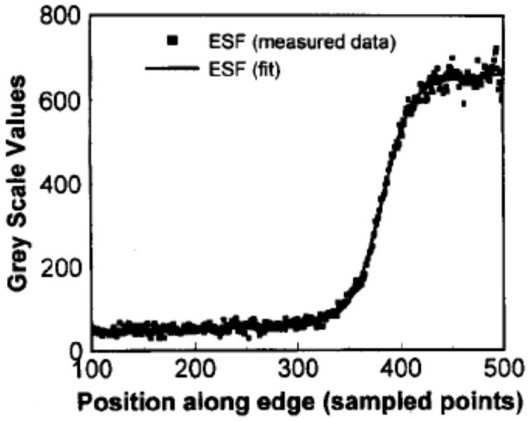

Figure 34 – Example of the intensity profile of a scan on a sharp edge. Image taken from ref.[131]

In order to obtain a rough estimation, I used a much more simpler approach based on the work of ref.[132]: since the LSF is an image of a line source, a rough estimation of it can be directly provided by a scan on a very sharp linear object, whose width can be considered negligible respect to the expected LSF/PSF.

Probes characterization

To best characterize the optical performance of the probes, I used various techniques exploiting the samples illustrated in the chapter “Test samples for BeMM and S-BeMM”. A lot of work has been done on fabricating test-samples with the right optical, topographical and mechanical properties. Here I show the results, obtained after having selected the correct optical techniques and test samples appropriate for my optical system.

BeMM probe

I focused myself on studying the optical properties of BeMM probe and its application for scanning Raman microscopy in reflection mode, where light illumination and collection are done by the same objective, and the bead is placed between the objective and the sample [see Figure 20(a)].

The laser focus position has to be optimized by matching two conditions: create the nanojet over the sample and efficiently collect the light that is reflected back or emitted, by the sample surface. In order to find the best condition, I used a configuration where the distances objective-bead and bead-sample was completely decoupled and I measured the intensity of the Rayleigh and Si Raman (at 521 cm^{-1}) peaks as a function of the focus point vertical position.

The Rayleigh signal shows some back reflections due to the several surfaces encountered by the laser beam, but is clearly visible only one peak of the Raman signal that comes from the sample surface. Figure 35(a) shows the intensity of Raman and Rayleigh signals according to the height of the objective with respect to the sample. During these measurements, the bead is steady in contact with the sample.

In such way is possible to identify the best alignment for collecting the Raman signal when the bead is scanning the sample surface. This configuration is obtained when the laser is focused at -3.8 µm, below the substrate. A negative value is the explanation of the fact that the perceived point of origin of the surface image appears to be located under the real position, in this situation a virtual image of the contact point is created. This image shifted from the real object is created by the micro lens effect [Figure 35(b)].

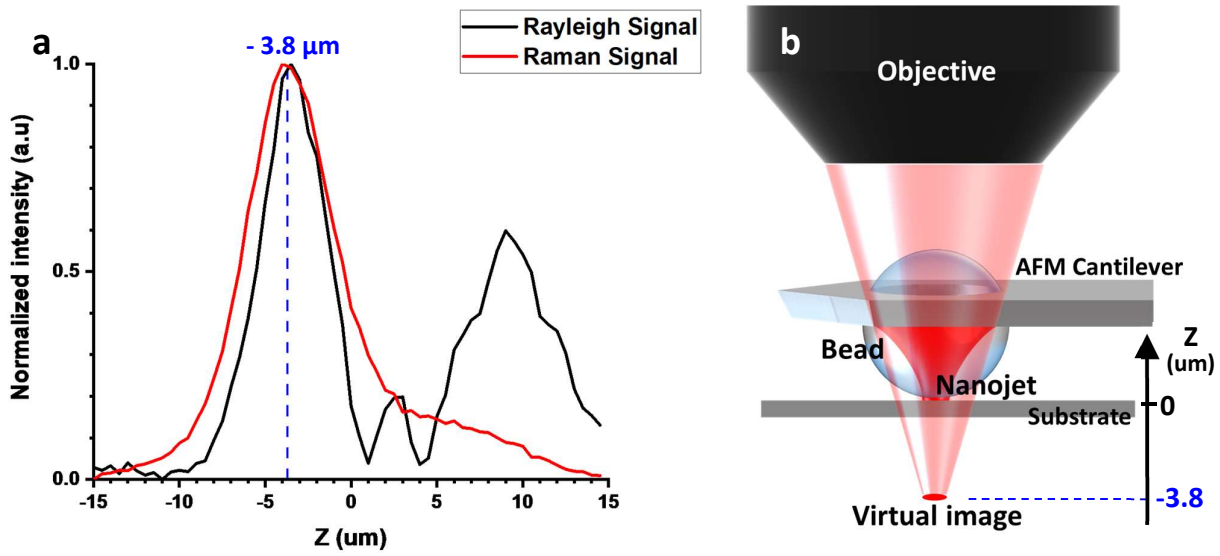

Figure 35 – a) intensity profile of the Raman and Rayleigh signals according to the position of the objective. Zero is set where the laser is focused directly onto the sample without the bead. b) Scheme (not in scale) of the configuration that collects the maximum Raman signal from the sample surface: the objective collects the virtual image of the sample from 3.8 µm below the sample. Bead diameter equal to 4.9 µm.

For a first rough estimation of the resolving power of the BeMM system, I measured a sample, lattice, formed by a layer of gold evaporated on glass and then milled by the FIB. In this way I obtained a lattice formed by a regular and net series of lines 200 nm wide with a period of 400 nm. In Figure 36, I show a test executed on this gold grating.

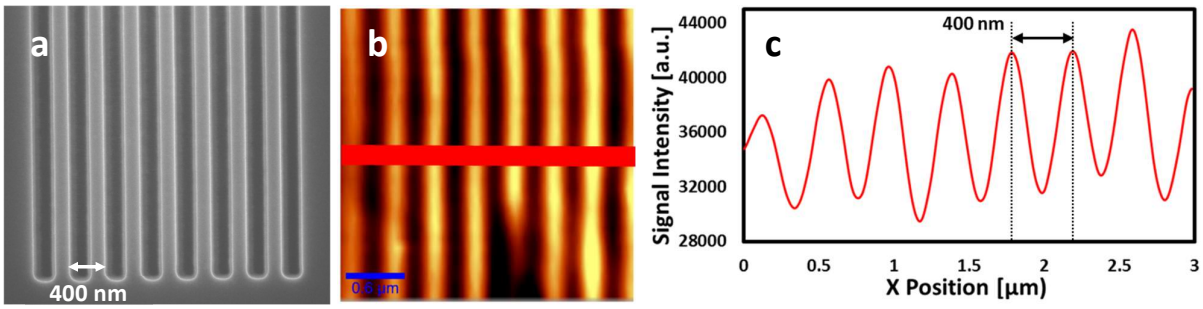

Figure 36 – a) SEM image of an Au grating with 400 nm pitch b) Optical map collected by BeMM probe from the scanning process on the grating shown in figure a (scale bar 0.6 µm). c) A line profile extract from the previous panel following the over imposed red line.

The ratio between I_{min} and I_{max} is ≈ 0.76, hence lower than the Rayleigh one (0.81, see previous chapter). It means that the grating with a 400 nm pitch is well resolved and our BeMM resolution should be a little higher.

A powerful feature of BeMM technique is the capability to collect simultaneously topographic and optical maps, since the micro bead acts also as an AFM probe. Figure 37(b)

and Figure 37(c) show the two kind of information obtained from the same scan, respectively reflection and topography. Moreover, the noticeable improvement of optical spatial resolution obtained by the bead respect to the one obtained by the objective alone can be clearly seen comparing Figure 37(a) and Figure 37(b). From the images it is possible to extract the intensity line profiles on different zones. By analyzing the line profiles extracted from two different zones of the sample it is easy to evaluate how the resolutions of the two optical systems are different, I show an example of such analysis in Figure 37(d) and Figure 37(e).

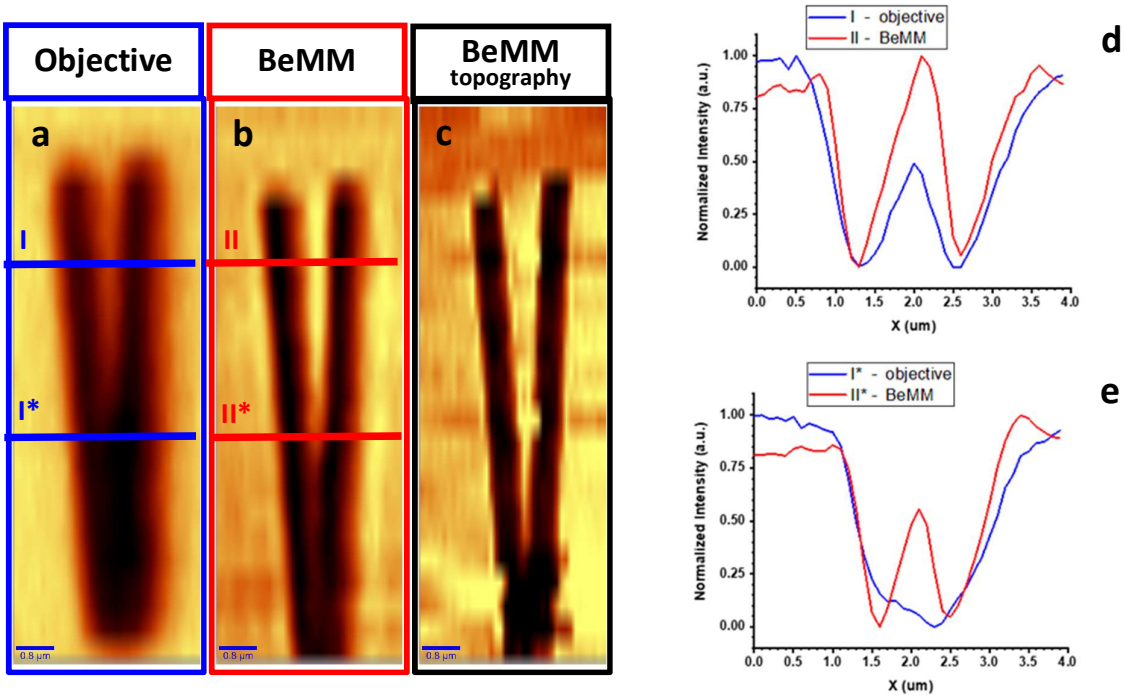

Figure 37 – a) Optical map of a V shape pattern (stripes width = 500 nm, angle = 6°) on a Si substrate covered with chromium, collected by a 50X objective (nominal NA 0.5). b) Optical map collected by a BeMM probe (4.9 µm silica bead) in contact with the surface. c) Topographic map created by the bead acting as AFM probe. d) Intensity profiles along lines I and II (stripes separation ≈ 1 µm), respectively in Figure a) and in Figure b). e) Intensity profiles along lines I and II* (stripes separation ≈ 500 nm), respectively in Figure a) and in Figure b).*

Although it was also possible to carry out a more quantitative study of the resolving power, for a more quantitative and precise analysis of the performance of the BeMM system, I decided to adopt other methods.

In order to better evaluate system capability with Raman signals, I fabricated and analyzed a specific Raman sample. This sample consists in a silicon substrate covered with 15 nm of chromium as covering layer and afterwards patterned with FIB to create 30 nm wide trenches. We can consider trenches width negligible, because is less than one order of magnitude respect to our expected PSF.

The Si Raman signal (at 521 cm^{-1}) has been collected under above illumination with a HeNe laser (λ = 633nm). I plotted the intensity profile of the Si Raman signal collected from patterned lines and I fitted the obtained PSF with a Gaussian equation as explained in previous chapter.

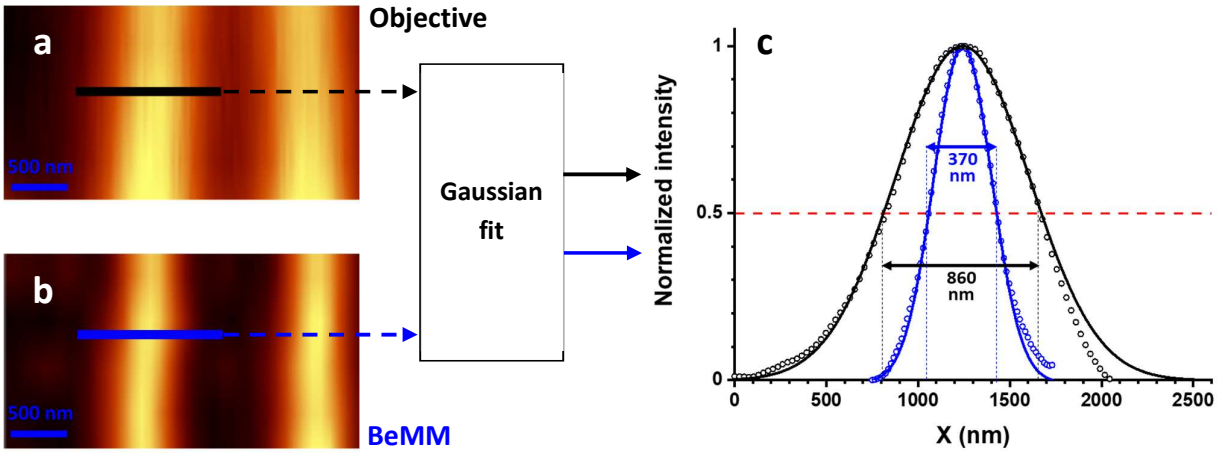

Figure 38 – a) Optical map of Si Raman peak wavenumber 521 cm^{-1} from 30 nm wide stripes, collected by a 50x objective (nominal NA 0.5). The distance between stripes is of 1.5 µm. b) Optical map of Si Raman peak wavenumber 521 cm^{-1} from 30 nm wide stripes, collected by a 4.9 µm silica bead in contact with the surface. c) Black line: calculated PSF of a 50x objective (nominal NA 0.5), making the Gaussian fitting of the intensity profile of the black area in figure a. Measured NA: 0.4. Blue line: calculated PSF of a 4.9 µm silica bead in contact with the surface, making the Gaussian fitting of the intensity profile of the blue area in figure b. Measured NA: 0.94.

The calculated FWHM of the PSF is than equal to 370 nm. According with the calculations about Rayleigh criterion shown in previous chapter, BeMM resolution is 370 × 1.12 ≈ 410 nm. It's a value comparable to the one obtained in grating experiment (≲ 400 nm).

This means an NA of 0.94 for the whole system, according with Rayleigh limit formula $(R = (0.61 \cdot \lambda)/N.A.)$ and for the wavelength of 633 nm used for these experiments. The NA is similar to the one (NA of 0.95) found by resolution studies conducted with these system and same microbeads.[12] The resolution obtained by the 50X objective (nominal N.A. 0.5) results to be 860 × 1.12 ≈ 960 nm (real N.A. 0.4). The PSF FWHM, and consequently the spatial resolution of the system, has improved by 2.3 times respect to the one without the bead.

S-BeMM probe

To extend furthermore the usage of Bead probes, obtain spatial super resolution and perform near field microscopy, I developed an evolution of BeMM that I call SNOM Bead Mediated Microscopy (S-BeMM). As I have already introduced in the chapter "S-BeMM probe fabrication" on fabrication methods, the new probe consists of a standard BeMM probe covered with 50 nm of aluminum with a tiny hole, around 40 nm, in the area of nano-jet.

As BeMM, also S-BeMM is designed to reproduce simultaneously a topographic and optical map of the sample under investigation. Figure 39 shows the two kind of information obtained from the same scan, respectively topography and reflection, performed onto a sharp border patterned in a 15 nm gold film onto a glass coverslip.

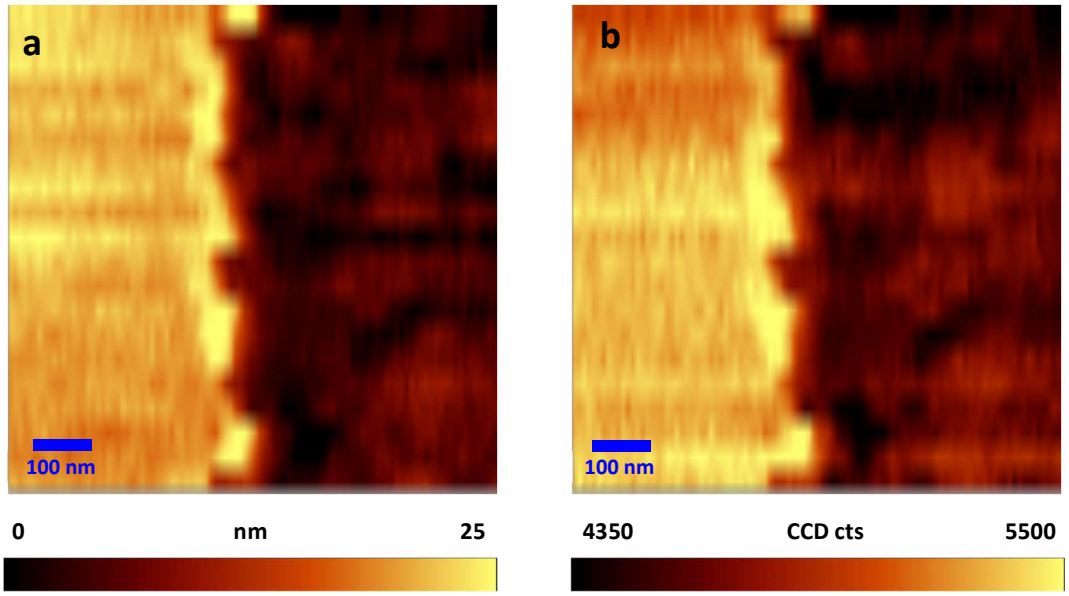

Figure 39 – a) Topographic map of a border patterned in a gold film onto a glass substrate, created by a S-BeMM probe in contact with the surface. b) Reflection map simultaneously collected by the same probe.

As the potential of S-BeMM probe may already be clear from the previous picture, an accurate characterization is required in order to evaluate spatial resolution. I calculated it with the technique of the knife-edge, as discussed in the previous chapter. This technique requires an extremely sharp edge with high optical contrast. I performed a fine scan with a resolution of 5 nm/point and a speed of 50 nm/s on a sharp edge obtained cutting by FIB a 15 nm chromium layer deposited onto a glass substrate (Figure 40).

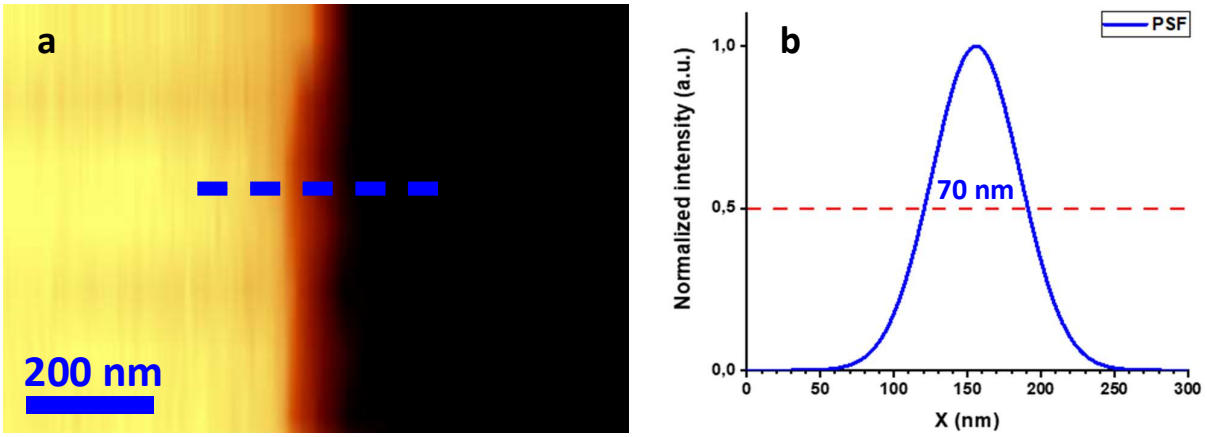

Figure 40 – a) Reflection signal map of a sharp edge of chromium/glass, collected with S-BeMM probe with hole of 40 nm. b) Calculated PSF probe by the derivative of the intensity profile taken along the blue line in a) as explained in previous chapter.

Similar to the previous chapter, from the analysis of the line profile I have therefore extracted the PSF width. These calculations indicate a PSF with a FWHM of 70 nm. According with Rayleigh criterion, S-BeMM spatial resolution is 70 × 1.12 ≈ 80 nm, which is λ/8 (excitation laser λ ≈ 632.8 nm). Only by comparison, according to the Rayleigh criterion ($R = 0.61 \cdot \lambda / NA$), an ideal perfect objective in air (NA = 0.9) reaches values around 430 nm while an oil objective with NA of 1.49, ideally, could reaches 290 nm.

Rayleigh scattering is an optical signal that is particularly easy to handle, because of his great intensity and simple spectroscopic properties (same λ of excitation light). Things get more difficult when we want to treat optically active samples, like fluorescent ones or Raman samples.

BeMM for fluorescence

Fluorescence signal is spectrally much easier to identify and it's much more intense than a Raman signal, thus the collection system can be less performing in terms of sensitivity and filters spectral quality. For this reason I started to fabricate and analyze fluorescent samples.

The first tests on these types of signals were carried out using fluorescent beads (see chapter "Fluorescent samples"). In Figure 41 I show some fluorescence maps of this kind of sample, taken with S-BeMM probe. They clearly show the characteristics of the sample with the typical bead cluster stripes. We can see that some beads are more intense than others, this is probably due to two main effects: the natural distribution in diameter and fluorescence of the beads and the uncontrolled, and therefore different, distance of the beads from the surface of the sample.

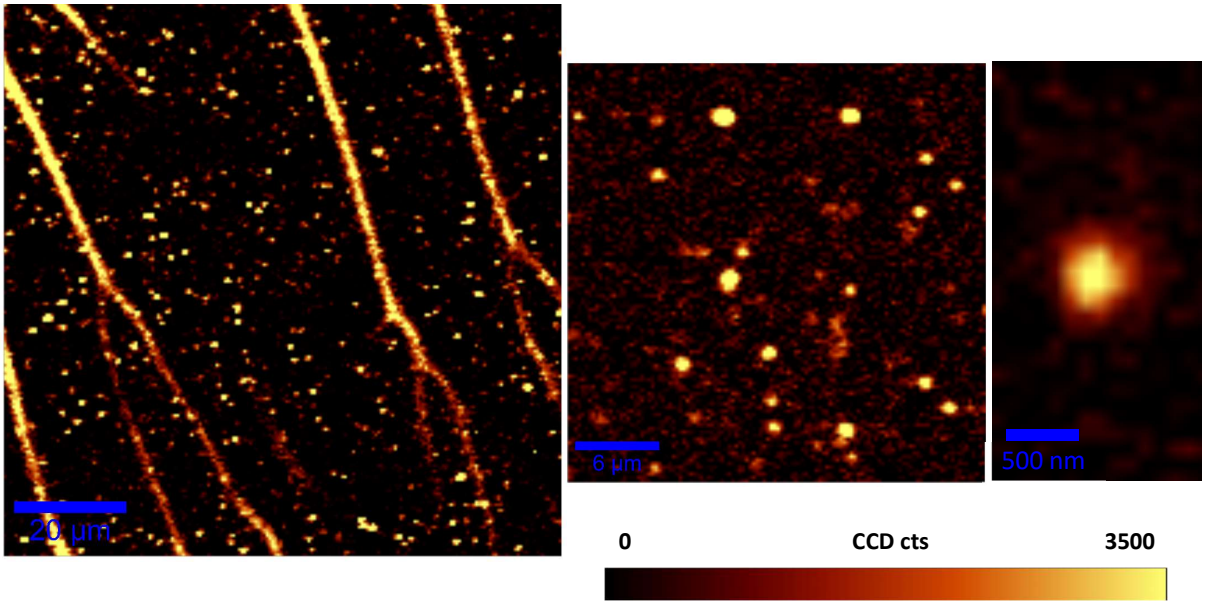

Figure 41 – Fluorescence maps at different magnification of areas of the fluorescent sample, created integrating the spectral signal between 670 nm and 690 nm, collected with S-BeMM probe with hole of 40 nm.

The maps show that S-BeMM can easily detect these fluorescent particles, allowing to scan a big area of hundreds of microns, with the sensibility to detect single particles with an appreciable spatial resolution. Unfortunately, it is quite evident that with this sample we are not in the nanometric near-field regime, because the particles appear definitely larger than the PSF calculated in previous experiments. Their mapped dimension is instead compatible with the PSF calculated for the BeMM probe. The problem could arise from that the resist film has a thickness around 200 nm, while the particles have a dimension of 40 nm. This caused an uncontrollable distribution of the nanobeads along the Z axis and clearly randomly far from the surface. By its nature, SNOM microscopy is a purely superficial investigation technique. Its main component, the near field, quickly extinguishes in the first layers below the surface (see Figure 7) leaving space for the far filed component. The latter is a propagating component that has no spatial confinement and, therefore, doesn't carry the desired resolution capacity. Unfortunately, I didn't managed to obtain a thinner layer, so I moved to a more flat kind of sample, also introducing a much more difficult class of signal: the Raman scattering.

Nano-scale Raman analysis

In order to go deeper in the application range and characterization, I decided to apply the S-BeMM technique on a sample formed by CNTs. By doing this I was not only able to test real samples with features at nanoscale but also to study in more detail the Raman spectroscopy

capabilities of the S-BeMM technique. CNTs Raman properties are introduced in previous chapter.

After preparing the sample as described in the previous chapter, I made a parallel analysis with confocal standard microscopy and S-BeMM microscopy technique.

I used as objective an Olympus LMPLFLN 50x (NA 0.5) for the confocal microscopy tests, and the same objective was then used as well to collect the output signal from the probe. The confocality was given by the collection optical fiber diameter that was 100 µm.

In Figure 42 I show as a typical images sequence for comparison: SEM image of some bundles of CNTs, their Raman spectrum collected with S-BeMM probe and, on the same area, I was able to collect the Raman signal with a standard confocal microscope and with S-BeMM probe in contact mode. Both scans have been performed at the maximum laser power, 35 mW, with an integration time of 0.2 s and a scan speed of 650 nm/sec.

The bead is definitely able to collect Raman signal even from nanoscale featured samples, as we already seen previously, resolving spatial features much better than the objective, maintaining an intense signal that is of the same order of magnitude than the one collected without the probe.

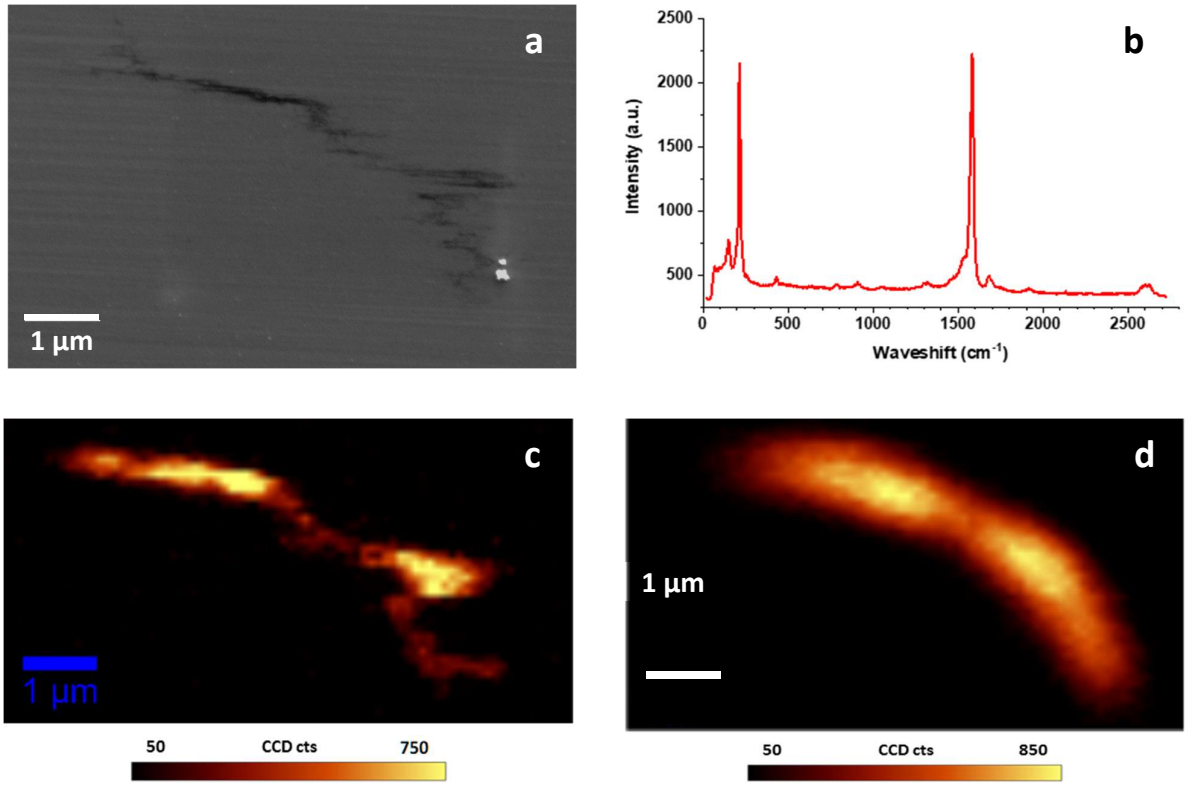

Figure 42 – On the same bundle of SWCNTs: a) SEM image. b) Raman spectrum collected with a S-BeMM probe (nanohole Ø = 60 nm); integration time 0.2 s. c) Optical map of Raman signal, integrated between 1550 and 1600 cm^{-1}, collected with a S-BeMM probe (nanohole Ø = 40 nm); integration time 0.2 s. d) Optical map of Raman signal (1550-1600 cm^{-1}) collected with a 50X objective; integration time 0.2 s.

Thanks to the system capabilities, it was possible to zoom in on the area of interest in order to collect, with high resolution, more detailed data. As an example, high spatial resolution Raman spectra can be extracted from the maps or, by selecting a specific peak or peaks (e.g. the previously introduced CNTs RBM), the evolution of it/them along a specific spatial line can be obtained.

In Figure 43(b), I summarize the results of this measurement with the Raman spectra in two different areas, A and B, and in Figure 43(c), the extracted intensity profile along the gray line overimposed on Figure 43(a) of the RMB peak identified at 255 cm^{-1}.

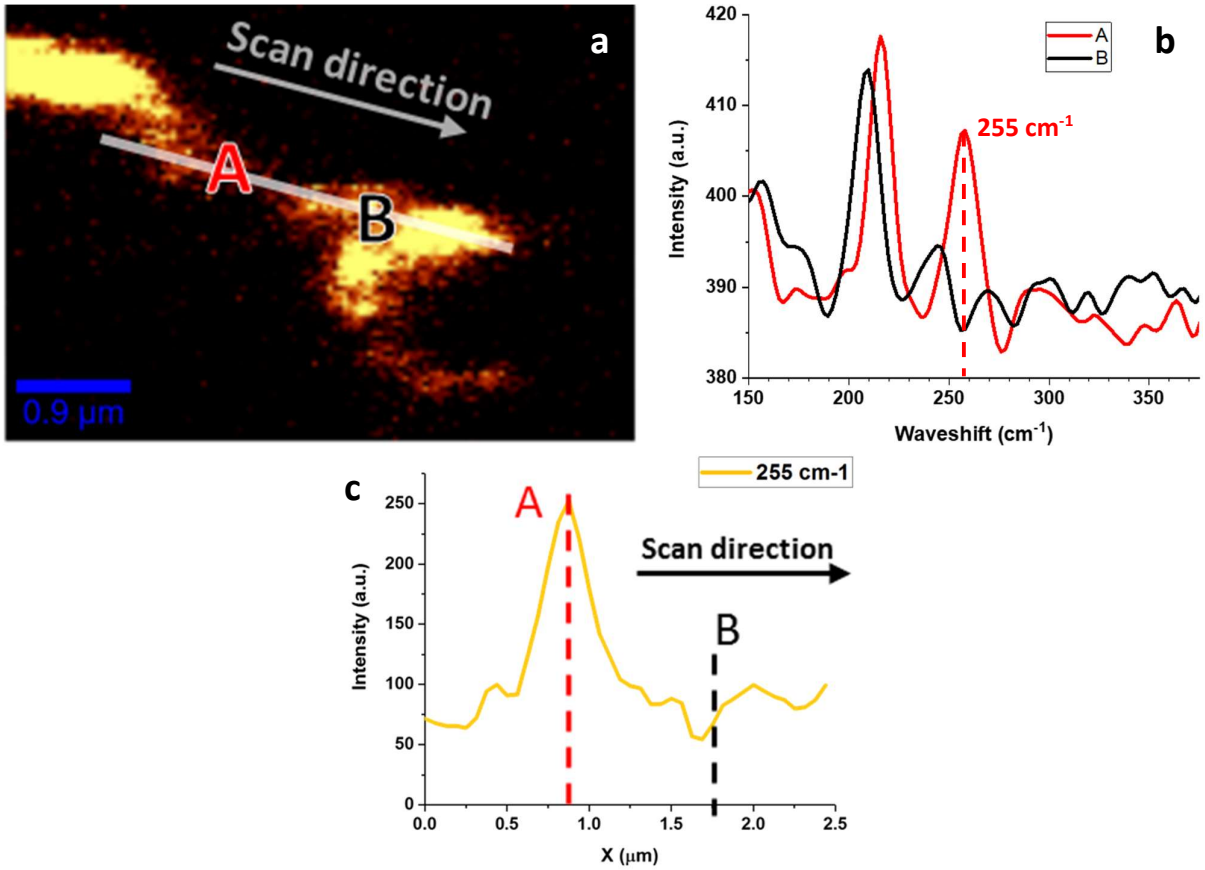

Figure 43 – a) Map of the SWCNTs bundle, Raman signal integrated in the band 1550-1600 cm^{-1}. The grey line highlights the path of a linear scan acquired at a longer integration time for higher spectral resolution. b) RBM peaks acquired in the A and B points in Figure a). c) Intensity profiles along the line in Figure a) of 255 cm^{-1} RBM peak.

From Figure 43(c) is quite evident that the RBM mode with the peak at 255 cm^{-1} has its maximum in position A and, after an evolution along the selected line, almost disappears in position B. Measuring the intensity of a Raman peak or its deviation from the reference value can provide important information on stress or other local phenomena affecting the

molecule/structure. In this light S-BeMM technique, with its high spatial resolution, acquires a position of interest in Raman spectroscopy of nanostructured surfaces.

The possibility of collecting, discriminating and creating maps of low intensity Raman modes opens up the possibility of analyzing the optical and geometric characteristics of CNTs using the BeMM technique. The same capability could be extended to a various range of nanoparticles as well as more optical features.

Conclusions and future perspectives

This dissertation collects the results obtained concerning several aspects of a new technique called Bead Mediated Microscopy (BeMM) and its evolution to near field, the Scanning Near Field Bead Mediated Microscopy (S-BeMM).

In BeMM technique a small bead of dielectric material is embedded in the optical lever of an AFM. Thanks to the optical properties of the bead and the accurate control of the probe movement of an AFM microscope, optical measurements can therefore be made.

The first step I made in my doctorate was to acquire and evolve the BeMM technique. I then took practice on its opto-mechanical system and studied the behavior of its main elements such as the AFM system, but especially the bead. I then took the steps for a further development of the technique, on the one hand, I looked for a simpler manufacture of the optical probes and, on the other hand, I tried to make test samples that would give me the key information required by the standard characterization techniques.

A great deal of effort has been put into the clean room business. Even if complex, my knowledge of lithographic and FIB/SEM techniques has allowed me to have samples of the highest manufacturing level, fundamental for a correct characterization of the optical system.

The possibility to scan in a controlled way the microbead over a sample enables to perform a detailed optical characterization of the resolution enhancement induced by the nanojet. The portable nanojet strategy presented here can be easily implemented in multiple applications where enhanced optical focusing can be advantageous, including imaging, lithography and Raman spectroscopy.

I have therefore focused my efforts more on Raman spectroscopy. As I was able to demonstrate in my PhD work, the BeMM system with its high numerical aperture and great collection efficiency is capable of mapping active Raman samples with spatial resolutions worthy of the best microscopes.

In order to go beyond the limit of diffraction it is necessary to change approach and exploit the so-called "near field" microscopy. The simplest near field source is a small aperture of a few tens of nm on an opaque screen. I then created a metal coating on the lower surface of the bead, and then generated a small aperture in the proximity of the nanojet. I was able to create a combination between the SNOM technique and the BeMM, a technique I called S-BeMM.

While the evolution of the S-BeMM system was almost a natural step of technological evolution, it also required me to carry out an advanced study of modern optical techniques in the near field. The clean room part also required a further effort, the new S-BeMM probe

required specific characteristics of the metal coating; characteristics of resistance to rubbing and to the high optical power density that is created in nanojet/nanoaperture.

The optical characterization of the S-BeMM technique showed a "sub diffraction limited" PSF comparable with the opening diameters generated on the coating, which was perfectly in line with the other SNOM opening techniques. But that's not all, the use of the bead as an optical lens/concentrator means that the high power density is concentrated only in the nanojet area and high input power can be used without damaging the probe. The possibility of using high power and therefore high power densities has opened the way for the application of such probes also with Raman technique. The use of S-BeMM on samples formed by CNT has in fact made it possible to highlight how the technique is not only capable of generating nanoscale resolution maps, but also allows local information on the chemical components and local stresses of the sample under investigation.

Despite the remarkable results achieved and the great applications of the technique, there is still room for evolution. In fact, the great density of localized power could still be used to excite plasmonic structures such as planar antennas or off-plane antennas, made in correspondence with the probe opening. In this way we could have more intense and even more localized EM fields, bringing the S-BeMM closer to the TERS technique.

The integration of S-BeMM system in a commercial AFM instrument permits to obtain super resolution chemical maps of specimens with high sensitivity. All these features are implemented in a rather simple design, allowing the possibility to produce an easy-to-use probe whose fabrication can be relatively cheap. Of course, these properties are important for any outlook towards a potential market.

List of Abbreviations

AFM	Atomic Force Microscopy/Microscope
BeMM	Bead Mediated Microscopy
CCD	Charge-Coupled Device
CNT	Carbon NanoTube
EM	Electro-Magnetic
FIB	Focused Ion Beam
NA	Numerical Aperture
NF	Near Field
NMP	N-Methyl-2-Pyrrolidone
PMMA	Poly Methyl MethAcrylate
RBM	Radial Breathing Mode
S-BeMM	SNOM-Bead Mediated Microscopy
sCMOS	scientific Complementary Metal-Oxide-Semiconductor
SEM	Scanning Electron Microscopy/Microscope
SERS	Surface Enhanced Raman Spectroscopy
SNOM	Scanning Near-field Optical Microscopy
SPM	Scanning Probe Microscopy
SWCNT	Single-Walled Carbon NanoTube
TEM	Transmission Electron Microscopy/Microscope
TERS	Tip-Enhanced Raman Spectroscopy

References

1. D. L. Rousseau, R. P. Bauman, and S. P. S. Porto, "*Normal Mode Determination in Crystals*", J. Raman Spectrosc. **10,** 253–290 (1981).
2. S. Jimenez-Sandoval, "*Micro-Raman spectroscopy: A powerful technique for materials research*", Microelectronics J. **31,** 419–427 (2000).
3. J. R. Ferraro, K. Nakamoto, and C. W. Brown, "*Introductory Raman Spectroscopy*", North-holl. Math. Stud. (20053).
4. R. Krishna, T. J. Unsworth, and R. Edge, "*Raman Spectroscopy and Microscopy*", Ref. Modul. Mater. Sci. Mater. Eng. 1–15 (2016).
5. U. Dürig, D. W. Pohl, and F. Rohner, "*Near-field optical-scanning microscopy*", J. Appl. Phys. **59,** 3318–3327 (1986).
6. X. Shi, N. Coca-López, J. Janik, and A. Hartschuh, "*Advances in tip-enhanced near-field raman microscopy using nanoantennas*", Chem. Rev. **117,** 4945–4960 (2017).
7. Lord Rayleigh, "*Investigations in Optics, with special reference to the Spectroscope.*", Philos. Magaziine J. Sci. **8,** 261–274 (1879).
8. M. Born and E. Wolf, "*Principles of Optics - Electromagnetic theory of propagation, interference and diffraction of light*", (Pergamon Press Ltd, 1999).
9. A. V. Itagi and W. A. Challener, "*Optics of photonic nanojets*", J. Opt. Soc. Am. A **22,** 2847 (2005).
10. A. Devilez, B. Stout, N. Bonod, and E. Popov, "*Spectral analysis of three-dimensional photonic jets*", Opt. Express **16,** 14200 (2008).
11. A. Heifetz, S. C. Kong, A. V. Sahakian, A. Taflove, and V. Backman, "*Photonic nanojets*", J. Comput. Theor. Nanosci. **6,** 1979–1992 (2009).
12. M. Duocastella, F. Tantussi, A. Haddadpour, R. P. Zaccaria, A. Jacassi, G. Veronis, A. Diaspro, and F. De Angelis, "*Combination of scanning probe technology with photonic nanojets*", Sci. Rep. **7,** 1–7 (2017).
13. A. Jacassi, F. Tantussi, M. Dipalo, C. Biagini, N. Maccaferri, A. Bozzola, and F. De Angelis, "*Scanning Probe Photonic Nanojet Lithography*", ACS Appl. Mater. Interfaces **9,** 32386–32393 (2017).
14. "*What is Raman Spectroscopy?*", at https://www.edinst.com/blog/what-is-raman-spectroscopy
15. "*RP Photonics Encyclopedia - Raman spectroscopy*", at https://www.rp-photonics.com/raman_spectroscopy.html
16. S. Berweger and M. B. Raschke, "*Signal limitations in tip-enhanced Raman scattering: The challenge to become a routine analytical technique*", Anal. Bioanal. Chem. **396,**

115–123 (2010).

17. F. A. Jenkins and H. E. White, "*Fundamentals of Optics*",
18. E. Hecht, "*Optics*", (Pearsons Education, 2003).
19. J. E. Greivenkamp, "*Field Guide to Geometrical Optics*", (The Society of Photo-Optical Instrumentation Engineers, 2004).
20. Z. Chen, A. Taflove, and V. Backman, "*Photonic nanojet enhancement of backscattering of light by nanoparticles: a potential novel visible-light ultramicroscopy technique*", Opt. Express **12,** 1214 (2004).
21. X. Li, Z. Chen, A. Taflove, and V. Backman, "*Optical analysis of nanoparticles via enhanced backscattering facilitated by 3-D photonic nanojets*", Opt. Express **13,** 526 (2005).
22. P. Ferrand, J. Wenger, A. Devilez, M. Pianta, B. Stout, N. Bonod, E. Popov, and H. Rigneault, "*Direct imaging of photonic nanojets*", Opt. Express **16,** 6930 (2008).
23. A. Devilez, N. Bonod, J. Wenger, D. Gérard, B. Stout, H. Rigneault, and E. Popov, "*Three-dimensional subwavelength confinement of light with dielectric microspheres*", Opt. Express **17,** 2089 (2009).
24. A. Devilez, J. Wenger, B. Stout, and N. Bonod, "*Transverse and longitudinal confinement of photonic nanojets by compound dielectric microspheres*", Nanophotonic Mater. VI **7393,** 73930E (2009).
25. C. Liu, "*Ultra-elongated photonic nanojets generated by a graded-index microellipsoid*", Prog. Electromagn. Res. Lett. **37,** 153–165 (2013).
26. A. M. Kapitonov and V. N. Astratov, "*Observation of nanojet-induced modes with small propagation losses in chains of coupled spherical cavities*", Opt. Lett. **32,** 409 (2007).
27. S. Lecler, S. Haacke, N. Lecong, O. Crégut, J.-L. Rehspringer, and C. Hirlimann, "*Photonic jet driven non-linear optics: example of two-photon fluorescence enhancement by dielectric microspheres*", Opt. Express **15,** 4935 (2007).
28. K. J. Yi, H. Wang, Y. F. Lu, and Z. Y. Yang, "*Enhanced Raman scattering by self-assembled silica spherical microparticles*", J. Appl. Phys. **101,** (2007).
29. W. Wu, A. Katsnelson, O. G. Memis, and H. Mohseni, "*A deep sub-wavelength process for the formation of highly uniform arrays of nanoholes and nanopillars*", Nanotechnology **18,** (2007).
30. H. Bethe, "*Theory of Diffraction by Small Holes*", Phys. Rev. **66,** 163–182 (1944).
31. C. J. Bouwkamp, "*On Bethe's theory of diffraction by small holes*", in (1950).
32. D. Van Labeke, D. Barchiesi, and F. Baida, "*Optical characterization of nanosources used in scanning near-field optical microscopy*", J. Opt. Soc. Am. A **12,** 695 (1995).
33. Z. L. Wang, M. Zhou, C. Y. Gao, and W. Zhang, "*Near-field properties of diffraction*

through a circular subwavelength-size aperture", Chinese Phys. B **21,** (2012).

34. B. Hecht, B. Sick, U. P. Wild, V. Deckert, R. Zenobi, O. J. F. Martin, and D. W. Pohl, "*Scanning near-field optical microscopy with aperture probes: Fundamentals and Applications*", J. Chem. Phys. **112,** 7761–7774 (2000).
35. H. Levine and J. Schwinger, "*On the theory of electromagnetic wave diffraction by an aperture in an infinite plane conducting screen*", Commun. Pure Appl. Math. **3,** 355–391 (1950).
36. J. W. Goodman, "*Introduction to Fourier Optics*", McGraw-Hill Ser. Electr. Comput. Eng. (1968).
37. O. J. F. Martin, C. Girard, and A. Dereux, "*Dielectric versus topographic contrast in near-field microscopy*", J. Opt. Soc. Am. A **13,** 1801 (1996).
38. M. W. Kowarz, "*Homogeneous and evanescent contributions in scalar near-field diffraction*", Appl. Opt. **34,** 3055 (1995).
39. H. Heinzelmann, B. Hecht, L. Novotny, and D. W. Pohl, "*Forbidden light scanning near-field optical microscopy*", J. Microsc. **177,** 115–118 (1995).
40. B. Hecht, H. Bielefeldt, D. W. Pohl, L. Novotny, and H. Heinzelmann, "*Influence of detection conditions on near-field optical imaging*", J. Appl. Phys. **84,** 5873–5882 (1998).
41. B. Hecht, H. Bielefeldt, L. Novotny, Y. Inouye, and D. W. Pohl, "*Local Excitation, Scattering, and Interference of Surface Plasmons*", Phys. Rev. Lett. **77,** 1889–1892 (1996).
42. W. E. Moerner, T. Plakhotnik, T. Irngartinger, U. P. Wild, D. W. Pohl, and B. Hecht, "*Near-field optical spectroscopy of individual molecules in solids*", Phys. Rev. Lett. **73,** 2764–2767 (1994).
43. A. L. Lereu and P. Dumas, "*Evolution of near field optical microscopy*", (2010).
44. B. Hecht, H. Bielefeldt, Y. Inouye, D. W. Pohl, and L. Novotny, "*Facts and artifacts in near-field optical microscopy*", J. Appl. Phys. **81,** 2492–2498 (1997).
45. E. Betzig, P. L. Finn, and J. S. Weiner, "*Combined shear force and near-field scanning optical microscopy*", Appl. Phys. Lett. **60,** 2484–2486 (1992).
46. R. Toledo-Crow, P. C. Yang, Y. Chen, and M. Vaez-Iravani, "*Near-field differential scanning optical microscope with atomic force regulation*", Appl. Phys. Lett. **60,** 2957–2959 (1992).
47. K. Karrai and R. D. Grober, "*Piezoelectric tip-sample distance control for near field optical microscopes*", Appl. Phys. Lett. 1842 (1995).
48. D. W. Pohl, W. Denk, and M. Lanz, "*Optical stethoscopy: Image recording with resolution λ/20*", Appl. Phys. Lett. **44,** 651–653 (1984).
49. K. Lieberman and A. Lewis, "*Simultaneous scanning tunneling and optical near-field*

imaging with a micropipette", Appl. Phys. Lett. **62,** 1335–1337 (1993).

50. M. Garcia-Parajo, E. Cambril, and Y. Chen, "*Simultaneous scanning tunneling microscope and collection mode scanning near-field optical microscope using gold coated optical fiber probes*", Appl. Phys. Lett. **65,** 1498–1500 (1994).

51. G. Binnig, C. F. Quate, and C. Gerber, "*Atomic force microscope*", Phys. Rev. Lett. **56,** 930–933 (1986).

52. T. A. Yano, Y. Inouye, and S. Kawata, "*Nanoscale uniaxial pressure effect of a carbon nanotube bundle on tip-enhanced near-field Raman spectra*", Nano Lett. **6,** 1269–1273 (2006).

53. N. Hayazawa, M. Motohashi, Y. Saito, H. Ishitobi, A. Ono, T. Ichimura, P. Verma, and S. Kawata, "*Visualization of localized strain of a crystalline thin layer at the nanoscale by tip-enhanced Raman spectroscopy and microscopy*", J. Raman Spectrosc. **38,** 684–696 (2007).

54. T. Schmid, A. Messmer, B. S. Yeo, W. Zhang, and R. Zenobi, "*Towards chemical analysis of nanostructures in biofilms II: Tip-enhanced Raman spectroscopy of alginates*", Anal. Bioanal. Chem. **391,** 1907–1916 (2008).

55. W. Scholz, C. Mihalcea, S. Werner, S. Muenster, and E. Oesterschulze, "*Novel micromachined cantilever sensors for scanning nearfield microscopy*", Scanning **18,** 157–158 (1996).

56. W. Noell, M. Abraham, K. Mayr, A. Ruf, J. Barenz, O. Hollricher, O. Marti, and P. Güthner, "*Micromachined aperture probe tip for multifunctional scanning probe microscopy*", Appl. Phys. Lett. **70,** 1236–1238 (1997).

57. E. Betzig, M. Isaacson, and A. Lewis, "*Collection mode near-field scanning optical microscopy*", Appl. Phys. Lett. **51,** 2088–2090 (1987).

58. E. Betzig, J. K. Trautman, T. D. Harris, J. S. Weiner, and R. L. Kostelak, "*Breaking the diffraction barrier: Optical microscopy on a nanometric scale*", Science (80-.). **251,** 1468–1470 (1991).

59. N. F. Van Hulst, M. H. P. Moers, O. F. J. Noordman, R. G. Tack, F. B. Segerink, and B. Bölger, "*Near-field optical microscope using a silicon-nitride probe*", Appl. Phys. Lett. **62,** 461–463 (1993).

60. L. Novotny and B. Hecht, "*Principles of Nano-Optics*", (Cambridge University Press, 2006).

61. K. B. Song, E. K. Kim, S. Q. Lee, J. Kim, and K. H. Park, "*Fabrication of a high-throughput cantilever-style aperture tip by the use of the bird's-beak effect*", Japanese J. Appl. Physics, Part 1 Regul. Pap. Short Notes Rev. Pap. **42,** 4353–4356 (2003).

62. P. N. Minh, T. Ono, and M. Esashi, "*High throughput aperture near-field scanning optical microscopy*", Rev. Sci. Instrum. **71,** 3111–3117 (2000).

63. A. Naber, D. Molenda, U. C. Fischer, H. J. Maas, C. Höppener, N. Lu, and H. Fuchs, "*Enhanced light confinement in a near-field optical probe with a triangular aperture*", Phys. Rev. Lett. **89,** 2108011–2108014 (2002).

64. G. C. Des Francs, D. Molenda, U. C. Fischer, and A. Naber, "*Enhanced light confinement in a triangular aperture: Experimental evidence and numerical calculations*", Phys. Rev. B - Condens. Matter Mater. Phys. **72,** (2005).

65. V. Sandoghdar and J. Mlynek, "*Prospects of apertureless SNOM with active probes*", J. Opt. A Pure Appl. Opt. **1,** 523–530 (1999).

66. J. Michaelis, C. Hettich, J. Mlynek, and V. Sandoghdar, "*Optical microscopy using a single-molecule light source*", Nature **405,** 325–328 (2000).

67. S. J. Erik, L. Novotny, and X. S. Xie, "*Near-field fluorescence microscopy based on two-photon excitation with metal tips*", Phys. Rev. Lett. **82,** 4014–4017 (1999).

68. Y. Kawata, C. Xu, and W. Denk, "*Feasibility of molecular-resolution fluorescence near-field microscopy using multi-photon absorption and field enhancement near a sharp tip*", J. Appl. Phys. **85,** 1294–1301 (1999).

69. A. V. Zayats and V. Sandoghdar, "*Apertureless scanning near-field second-harmonic microscopy*", Opt. Commun. **178,** 245–249 (2000).

70. A. V. Zayats and V. Sandoghdar, "*Apertureless near-field optical microscopy via local second-harmonic generation*", J. Microsc. **202,** 94–99 (2001).

71. A. Cricenti, "*Scanning Near-Field Optical Microscopy*", Encycl. Condens. Matter Phys. **8,** 163–171 (2005).

72. L. Novotny and C. Hafner, "*Light propagation in a cylindrical waveguide with a complex, metallic, dielectric function*", Phys. Rev. E **50,** 4094–4106 (1994).

73. A. H. La Rosa, B. I. Yakobson, and H. D. Hallen, "*Origins and effects of thermal processes on near-field optical probes*", Appl. Phys. Lett. **67,** 2597 (1995).

74. D. I. Kavaldjiev, R. Toledo-Crow, and M. Vaez-Iravani, "*On the heating of the fiber tip in a near-field scanning optical microscope*", Appl. Phys. Lett. **67,** 2771 (1995).

75. M. Stähelin, M. A. Bopp, G. Tarrach, A. J. Meixner, and I. Zschokke-Gränacher, "*Temperature profile of fiber tips used in scanning near-field optical microscopy*", Appl. Phys. Lett. **2603,** 2603 (1995).

76. C. Lienau, A. Richter, and T. Elsaesser, "*Light-induced expansion of fiber tips in near-field scanning optical microscopy*", Appl. Phys. Lett. **69,** 325–327 (1996).

77. L. Novotny, D. W. Pohl, and B. Hecht, "*Scanning near-field optical probe with ultrasmall spot size*", Opt. Lett. **20,** 970 (1995).

78. C. J. Bouwkamp, "*Diffraction theory*", Reports Prog. Phys. **17,** 35–100 (1954).

79. D. Kazantsev, G. Guttroff, M. Bayer, and A. Forchel, "*Sample temperature measurement in a scanning near-field optical microscope*", Appl. Phys. Lett. **72,** 689–

691 (1998).

80. P. G. Gucciardi, S. Patanè, A. Ambrosio, M. Allegrini, A. D. Downes, G. Latini, O. Fenwick, and F. Cacialli, "*Observation of tip-to-sample heat transfer in near-field optical microscopy using metal-coated fiber probes*", Appl. Phys. Lett. **86,** 1–3 (2005).

81. A. Ambrosio, O. Fenwick, F. Cacialli, R. Micheletto, Y. Kawakami, P. G. Gucciardi, D. J. Kang, and M. Allegrini, "*Shape dependent thermal effects in apertured fiber probes for scanning near-field optical microscopy*", J. Appl. Phys. **99,** (2006).

82. R. M. Stöckle, N. Schaller, V. Deckert, C. Fokas, and R. Zenobi, "*Brighter near-field optical probes by means of improving the optical destruction threshold*", J. Microsc. **194,** 378–382 (1999).

83. S. Ezugwu, H. Ye, and G. Fanchini, "*Three-dimensional scanning near field optical microscopy (3D-SNOM) imaging of random arrays of copper nanoparticles: Implications for plasmonic solar cell enhancement*", Nanoscale **7,** 252–260 (2015).

84. R. Bauld, M. Hesari, M. S. Workentin, and G. Fanchini, "*Thermal stability of Au25-molecular precursors and nucleation of gold nanoparticles in thermosetting polyimide thin films*", Appl. Phys. Lett. **101,** (2012).

85. R. M. Stöckle, Y. D. Suh, V. Deckert, and R. Zenobi, "*Nanoscale chemical analysis by tip-enhanced Raman spectroscopy*", Chem. Phys. Lett. **318,** 131–136 (2000).

86. N. Hayazawa, Y. Inouye, Z. Sekkat, and S. Kawata, "*Metallized tip amplification of near-field Raman scattering*", Opt. Commun. **183,** 333–336 (2000).

87. M. S. Anderson, "*Locally enhanced Raman spectroscopy with an atomic force microscope*", Appl. Phys. Lett. **76,** 3130–3132 (2000).

88. B. Pettinger, G. Picardi, R. Schuster, and G. Ertl, "*Surface Enhanced Raman Spectrscopy: Towards Single Molecule Spectroscopy*", Electrochemistry **68,** 942–949 (2000).

89. N. Kumar, S. Mignuzzi, W. Su, and D. Roy, "*Tip-enhanced Raman spectroscopy: principles and applications*", EPJ Tech. Instrum. **2,** (2015).

90. B. Pettinger, "*Single-molecule surface- and tip-enhanced Raman spectroscopy*", Mol. Phys. **108,** 2039–2059 (2010).

91. N. Mauser and A. Hartschuh, "*Tip-enhanced near-field optical microscopy*", Chem. Soc. Rev. **43,** 1248–1262 (2014).

92. P. Verma, "*Tip-Enhanced Raman Spectroscopy: Technique and Recent Advances*", Chem. Rev. **117,** 6447–6466 (2017).

93. F. Zenhausern, M. P. O'Boyle, and H. K. Wickramasinghe, "*Apertureless Near-Field Optical Microscope*", **65,** 1623–1625 (1994).

94. F. Zenhausern, Y. Martin, and H. K. Wickramasinghe, "*Scanning interferometric apertureless microscopy: Optical imaging at 10 angstrom resolution*", Science (80-.).

269, 1083–1085 (1995).

95. B. Ren, G. Picardi, and B. Pettinger, "*Preparation of gold tips suitable for tip-enhanced Raman spectroscopy and light emission by electrochemical etching*", Rev. Sci. Instrum. **75,** 837–841 (2004).

96. C. Williams and D. Roy, "*Fabrication of gold tips suitable for tip-enhanced Raman spectroscopy*", J. Vac. Sci. Technol. B Microelectron. Nanom. Struct. **26,** 1761 (2008).

97. S. S. Kharintsev, G. G. Hoffmann, A. I. Fishman, and M. K. Salakhov, "*Plasmonic optical antenna design for performing tip-enhanced Raman spectroscopy and microscopy*", J. Phys. D. Appl. Phys. **46,** (2013).

98. I. U. Vakarelski and K. Higashitani, "*Single-nanoparticle-terminated tips for scanning probe microscopy*", Langmuir **22,** 2931–2934 (2006).

99. H. Wang, T. Tian, Y. Zhang, Z. Pan, Y. Wang, and Z. Xiao, "*Sequential electrochemical oxidation and site-selective growth of nanoparticles onto AFM probes*", Langmuir **24,** 8918–8922 (2008).

100. X. Ma, M. Grüßer, and R. Schuster, "*Plasmonic nanospheres with a handle - Local electrochemical deposition of Au or Ag at the apex of optically inactive W- or C-tips*", Appl. Phys. Lett. **106,** (2015).

101. A. Taguchi, N. Hayazawa, Y. Saito, H. Ishitobi, A. Tarun, and S. Kawata, "*Controlling the plasmon resonance wavelength in metal-coated probe using refractive index modification*", Opt. Express **17,** 6509 (2009).

102. M. Asghari-Khiavi, B. R. Wood, P. Hojati-Talemi, A. Downes, D. McNaughton, and A. Mechler, "*Exploring the origin of tip-enhanced Raman scattering; Preparation of efficient TERS probes with high yield*", J. Raman Spectrosc. **43,** 173–180 (2012).

103. V. Deckert, T. Deckert-Gaudig, M. Diegel, I. Götz, L. Langelüddecke, H. Schneidewind, G. Sharma, P. Singh, P. Singh, S. Trautmann, M. Zeisberger, and Z. Zhang, "*Spatial resolution in Raman spectroscopy*", Faraday Discuss. **177,** 9–20 (2015).

104. T. L. Vasconcelos, B. S. Archanjo, B. Fragneaud, B. S. Oliveira, J. Riikonen, C. Li, D. S. Ribeiro, C. Rabelo, W. N. Rodrigues, A. Jorio, C. A. Achete, and L. G. Cançado, "*Tuning Localized Surface Plasmon Resonance in Scanning Near-Field Optical Microscopy Probes*", ACS Nano **9,** 6297–6304 (2015).

105. I. Maouli, A. Taguchi, Y. Saito, S. Kawata, and P. Verma, "*Optical antennas for tunable enhancement in tip-enhansed Raman spectroscopy imaging*", Appl. Phys. Express **8,** 2–4 (2015).

106. H. G. Frey, F. Keilmann, A. Kriele, and R. Guckenberger, "*Enhancing the resolution of scanning near-field optical microscopy by a metal tip grown on an aperture probe*", Appl. Phys. Lett. **81,** 5030–5032 (2002).

107. H. G. Frey, S. Witt, K. Felderer, and R. Guckenberger, "*High-resolution imaging of single fluorescent molecules with the optical near-field of a metal tip*", Phys. Rev. Lett. **93,** 1–

4 (2004).

108. S. Berweger, J. M. Atkin, R. L. Olmon, and M. B. Raschke, "*Adiabatic tip-plasmon focusing for nano-raman spectroscopy*", J. Phys. Chem. Lett. **1,** 3427–3432 (2010).

109. N. C. Lindquist, T. W. Johnson, P. Nagpal, D. J. Norris, and S. H. Oh, "*Plasmonic nanofocusing with a metallic pyramid and an integrated C-shaped aperture*", Sci. Rep. **3,** (2013).

110. "*All-In-One-Al-Tipless AFM Probe - BudgetSensors*", at https://www.budgetsensors.com/multipurpose-afm-probe-no-tip-all-in-one-al-tipless

111. "*Refractive index database*", at https://refractiveindex.info/

112. J. Maultzsch, S. Reich, and C. Thomsen, "*Raman scattering in carbon nanotubes revisited*", Phys. Rev. B - Condens. Matter Mater. Phys. **65,** 1–4 (2002).

113. S. Reich, C. Thomsen, and J. Maultzsch, "*Carbon Nanotubes*", (2004).

114. V. N. Popov, "*Carbon nanotubes: Properties and application*", Mater. Sci. Eng. R Reports **43,** 61–102 (2004).

115. F. Hennrich, R. Krupke, S. Lebedkin, K. Arnold, R. Fischer, D. E. Resasco, and M. M. Kappes, "*Raman spectroscopy of individual single-walled carbon nanotubes from various sources*", J. Phys. Chem. B **109,** 10567–10573 (2005).

116. P. Singh, S. Campidelli, S. Giordani, D. Bonifazi, A. Bianco, and M. Prato, "*Organic functionalisation and characterisation of single-walled carbon nanotubes*", Chem. Soc. Rev. **38,** 2214–2230 (2009).

117. S. Suzuki, "*Physical and Chemical Properties of Carbon Nanotubes*", (2013).

118. A. I. López-Lorente, B. M. Simonet, and M. Valcárcel, "*Raman spectroscopic characterization of single walled carbon nanotubes: Influence of the sample aggregation state*", Analyst **139,** 290–298 (2014).

119. S. Malola, H. Häkkinen, and P. Koskinen, "*Effect of bending on Raman-active vibration modes of carbon nanotubes*", Phys. Rev. B - Condens. Matter Mater. Phys. **78,** 2–5 (2008).

120. T. A. Yano, T. Ichimura, S. Kuwahara, F. H'Dhili, K. Uetsuki, Y. Okuno, P. Verma, and S. Kawata, "*Tip-enhanced nano-Raman analytical imaging of locally induced strain distribution in carbon nanotubes*", Nat. Commun. **4,** 1–7 (2013).

121. J. Maultzsch, H. Telg, S. Reich, and C. Thomsen, "*Radial breathing mode of single-walled carbon nanotubes: Optical transition energies and chiral-index assignment*", Phys. Rev. B - Condens. Matter Mater. Phys. **72,** 1–16 (2005).

122. "*High Resolution Raman Imaging of Carbon Nanotubes | Nanophoton corp*", at https://www.nanophoton.net/applications/nano-carbon/cnt-high-resolution

123. B. P. Ramsay, E. L. Cleveland, and O. T. Koppius, "*Criteria and the Intensity-Epoch*

Slope", J. Opt. Soc. Am. **31,** 26 (1941).

124. C. M. Sparrow, "*On Spectroscopic Resolving Power*", Am. Astron. Soc. **213,** 165 (1967).
125. "*Confocal and Two-Photon Microscopy: Foundations, Applications and Advances*", (2001).
126. R. Horstmeyer, R. Heintzmann, G. Popescu, L. Waller, and C. Yang, "*Standardizing the resolution claims for coherent microscopy*", Nat. Photonics **10,** 68–71 (2016).
127. B. Zhang, J. Zerubia, and J. C. Olivo-Marin, "*Gaussian approximations of fluorescence microscope point spread function models*", Appl. Opt. **46,** 1819–1829 (2007).
128. V. N. Mahajan, "*Unifrom versus Gaussiam Beams: a Comparison of the Effects of Diffraction, Obscuration, and Aberrations*", Ratio **3,** 470–485 (1986).
129. K. Rossmann, "*Point spread-function, line spread-function, and modulation transfer function. Tools for the study of imaging systems.*", Radiology **93,** 257–272 (1969).
130. J. A. Arnaud, W. M. Hubbard, G. D. Mandeville, B. de la Clavière, E. A. Franke, and J. M. Franke, "*Technique for Fast Measurement of Gaussian Laser Beam Parameters*", Appl. Opt. **10,** 2775 (1971).
131. J. M. Boone and J. A. Seibert, "*An Analytical Edge Spread Function Model for Computer Fitting And Subsequent Calculation of the LSF and MTF*", Med. Phys. **21,** 1541–1545 (1994).
132. G. D. Boreman, "*Modulation Transfer Function in Optical and Electro-Optical Systems*", (The Society of Photo-Optical Instrumentation Engineers, 2001).

Acknowledgements

I am extremely grateful to Università degli Studi di Genova, which evaluated me worthy for a scholarship that have allowed me to attend this PhD course.

I also wish to thank very much the Istituto Italiano di Tecnologia (IIT), where I spent these three years studying and working in order to expand my scientific knowledge.

I would like to extend my gratitude in particular to my PhD tutor, Dr. Francesco De Angelis, who welcomed me in Plasmon Nanotechnologies line and gave me means and methods to perform my research in the Raman Lab of IIT.

I want to express my special appreciation to Dr. Francesco Tantussi, researcher and chief technician of the Raman Lab in IIT, for his precious and patient guidance on optical instruments and techniques, and for having efficiently balanced encouragements and useful critiques about my research work, my results, and about the writing of my thesis.

I am deeply indebted to the Clean Room Facility coordinator Dr. Andrea Toma for having given me the opportunity to work for him as a technician during the final accomplishment of my thesis, and in general I want to highlight my great pleasure of working in the Facility for the fabrications, with the expert technical staff: Dr. Marco Leoncini, Dr. Fabio Moia and Dr. Eliana Rondanina.

In addition, I would like to thank my relatives for having always promoted my study path and for their profound belief in my career choices.

Finally, I very much appreciate the person who shares my time and energy with my job, my girlfriend Ilaria, because she helps me to maintain a good work-life balance and gives meaning to all my efforts.